

# Near-Infrared Survey of the GOODS-North Field: Search for Luminous Galaxy Candidates at $z \gtrsim 6.5$ <sup>\*†</sup>

Nimish P. Hathi<sup>1,2</sup>, Bahram Mobasher<sup>2</sup>, Peter Capak<sup>3</sup>, Wei-Hao Wang<sup>4</sup>,  
Henry C. Ferguson<sup>5</sup>

nhathi@obs.carnegiescience.edu

## ABSTRACT

We present near-infrared (NIR;  $J$  &  $K_s$ ) survey of the Great Observatories Origins Deep Survey-North (GOODS-N) field. The publicly available imaging data were obtained using the MOIRCS instrument on the 8.2m Subaru and the WIRCam instrument on the 3.6m Canada-France-Hawaii Telescope (CFHT). These observations fulfill a serious wavelength gap in the GOODS-N data - i.e., lack of deep NIR observations. We combine the Subaru/MOIRCS and CFHT/WIRCam archival data to generate deep  $J$  and  $K_s$  band images, covering the full GOODS-N field ( $\sim 169$  arcmin<sup>2</sup>) to an AB magnitude limit of  $\sim 25$  mag ( $3\sigma$ ). We applied  $z_{850}$ -band dropout color selection criteria, using the NIR data generated here. We have identified two possible Lyman Break Galaxy (LBG) candidates at  $z \gtrsim 6.5$  with  $J \lesssim 24.5$ . The first candidate is a likely LBG at  $z \simeq 6.5$  based on a weak spectral feature tentatively identified as Ly $\alpha$  line in the deep Keck/DEIMOS spectrum, while the second candidate is a possible LBG at  $z \simeq 7$  based on its photometric redshift. These  $z_{850}$ -dropout objects, if confirmed, are among the brightest such candidates found so far. At  $z \gtrsim 6.5$ , their

---

<sup>1</sup>Observatories of the Carnegie Institution for Science, Pasadena, CA 91101, USA

<sup>2</sup>Department of Physics and Astronomy, University of California, Riverside, CA 92521, USA

<sup>3</sup>Department of Astronomy, 249-17 Caltech, 1201 E. California Blvd., Pasadena, CA 91125, USA

<sup>4</sup>Institute of Astronomy and Astrophysics, Academia Sinica, P.O. Box 23-141, Taipei 10617, Taiwan

<sup>5</sup>Space Telescope Science Institute, 3700 San Martin Drive, Baltimore, MD 21218, USA

<sup>\*</sup>Based in part on data collected at Subaru Telescope, which is operated by the National Astronomical Observatory of Japan.

<sup>†</sup>Based on observations obtained with WIRCam, a joint project of CFHT, Taiwan, Korea, Canada, France, at the Canada-France-Hawaii Telescope (CFHT) which is operated by the National Research Council (NRC) of Canada, the Institut National des Sciences de l'Univers of the Centre National de la Recherche Scientifique of France, and the University of Hawaii.

star formation rate is estimated as  $100\text{--}200\text{ M}_\odot\text{ yr}^{-1}$ . If they continue to form stars at this rate, they assemble a stellar mass of  $\sim 5 \times 10^{10}\text{ M}_\odot$  after about 400 million years, becoming the progenitors of massive galaxies observed at  $z \simeq 5$ . We study the implication of the  $z_{850}$ -band dropout candidates discovered here, in constraining the bright-end of the luminosity function and understanding the nature of high redshift galaxies.

*Subject headings:* catalogs — galaxies:formation — galaxies:evolution — galaxies:high-redshift

## 1. Introduction

In recent times, the high redshift frontier has started to probe the epoch of reionization because of extensive observations at Near-Infrared (NIR) wavelengths. This extension of multi-wavelength galaxy surveys to obtain deep images at observed NIR has provided a new prospect for the study of galaxies at high ( $z \gtrsim 6.5$ ) redshifts. Such observations are vital to identify star-forming high redshift objects by sampling their rest-frame UV light, and for estimating their star formation properties. On the other hand, the combination of *Spitzer*/IRAC and NIR observations can be used to identify massive, evolved Balmer Break Galaxies (BBGs) at  $z \gtrsim 5$  (e.g., Wiklind et al. 2008). Furthermore, relative insensitivity at these wavelengths to the stellar population mix, dust and K-correction, specially at intermediate ( $z \simeq 2$ ) redshifts is an added bonus.

Among the most extensive datasets available in extragalactic astronomy, is the Great Observatories Origins Deep Survey (GOODS; Giavalisco et al. 2004a). This consists of imaging of two fields (GOODS-North and GOODS-South), by the *Hubble Space Telescope* (HST) Advanced Camera for Surveys (ACS) in four optical bands ( $B_{435}$ ,  $V_{606}$ ,  $i_{775}$ ,  $z_{850}$ ). Given the need for NIR data in any study of evolution of galaxies, the GOODS-South (GOODS-S) field has been observed extensively at NIR wavelengths, using the 8.2m Very Large Telescope (VLT; Renzini et al. 2003) in the  $J$ ,  $H$  and  $K_s$  bands, but the GOODS-North (GOODS-N) field has not had such full-field deep coverage at these wavelengths. In the last few years, the Wide-field InfraRed Camera (WIRCam; Puget et al. 2004) on the 3.6m Canada-France-Hawaii Telescope (CFHT), and the Multi-Object Infrared Camera and Spectrograph (MOIRCS; Ichikawa et al. 2006; Suzuki et al. 2008) on the 8.2m Subaru telescope have invested large amounts of observing time to obtain NIR observations of the GOODS-N field. The WIRCam  $K_s$  data were published by Wang et al. (2010) and the MOIRCS  $J$ ,  $H$ , and  $K_s$  data were published by Kajisawa et al. (2011). In both works, the images and catalogs were made publicly available. Various studies have used subsets of these observations for

specific science goals. For example, Kajisawa et al. (2006) used MOIRCS data to investigate the number counts of Distant Red Galaxies, while Ichikawa et al. (2007) used MOIRCS  $K_s$ -band selected galaxies to measure clustering properties of low-mass galaxies at  $1 < z < 4$ . Bundy et al. (2009) used NIR observations from both GOODS fields to investigate the dependence on stellar mass and galaxy type of the close pair fractions and implied merger rate, while Bouwens et al. (2008) used the deepest NIR observations from both fields to search for star-forming galaxies at  $z \gtrsim 6.5$  and constrain their rest-frame ultraviolet (UV) luminosity functions. These studies show the significance of NIR observations in such well-studied fields. The full coverage of the GOODS-N region is essential not only to expand these studies, but also to accomplish larger number of additional science goals. Despite such studies, there is limited information in literature of the observational details and sensitivities of the NIR data for GOODS-N field, and details about source detection.

The high sensitivity of the *HST*/Wide Field Camera 3 (WFC3) has made it possible to identify faint Lyman break galaxies (LBGs) at  $z \gtrsim 6.5$  (e.g., Oesch et al. 2010; Bouwens et al. 2010a,b; Finkelstein et al. 2010; Yan et al. 2010; Wilkins et al. 2011), when the universe was only about 500 Myr old. However, because most of these candidates are very faint ( $AB \gtrsim 27$  mag), it is difficult to measure their spectra or measure their rest-frame optical SEDs to better constrain their stellar population and mass. It is imperative to search for relatively brighter ( $AB \lesssim 25$  mag) galaxies at  $z \gtrsim 6.5$ , and study them in great detail. There are three principal ways to accomplish this goal. First approach is through big cluster surveys, which are searching for lensed galaxies at  $z \gtrsim 6.5$  (e.g., Hall et al. 2012; Bradley et al. 2012). These galaxies are intrinsically faint but because of the magnification their observed magnitudes are relatively bright. Second approach is to take advantage of the *HST* parallel observations (e.g., Trenti et al. 2011; Yan et al. 2011) to explore large number of random fields at relatively shallow depth, and the final approach is to perform wide area ground-based surveys (e.g., Ouchi et al. 2009; Castellano et al. 2010; Hickey et al. 2010; Capak et al. 2011) to identify and study such bright candidates. These methods are starting to identify bright galaxy candidates at  $z \gtrsim 6.5$  and are putting important constraints on the bright end of the rest-frame UV luminosity functions, though the number of these candidates remains too small to make any statistically significant conclusions about their physical properties.

The wide area ground-based surveys have few distinct advantages compared to space-based approaches of identifying bright high redshift ( $z \gtrsim 6.5$ ) galaxies. First, they can cover much larger area than space-based observations, and secondly, the  $K_s$ -band data, which is important for accessing the reliability of high redshift candidates, is only available through ground-based telescopes. These reasons make NIR ground-based surveys very appealing for searching bright high redshift galaxies.

Here, we present NIR data in the GOODS-N field obtained using the CFHT/WIRCam and the Subaru/MOIRCS instruments. We combine the archival data from these instruments to generate deeper images in  $J$ - and  $K_s$ -bands. The Subaru/MOIRCS data cover  $\sim 60\%$  of the central GOODS-N region in  $J$ ,  $H$ ,  $K_s$ -filters, while the CFHT/WIRCam covers a much larger area, extending well beyond the GOODS-N field in the  $J$ ,  $K_s$ -filters. The combination of the MOIRCS and WIRCam NIR data covers full area of the GOODS-N field ( $\sim 169$  arcmin<sup>2</sup>), and is deeper in the central  $\sim 60\%$  of the field. These combined images will extend far beyond the traditional field which the *HST*/WFC3 data will cover, and will considerably help to undertake multi-wavelength science goals that require NIR observations. As one application, here we use these NIR images along with the *HST*/ACS  $B_{435}$ ,  $V_{606}$ ,  $i_{775}$ ,  $z_{850}$  data to identify bright  $z_{850}$ -dropouts (i.e., LBG candidates at  $z \gtrsim 6.5$ ), and estimate their surface density in the GOODS-N field at the brighter limits ( $AB < 25$  mag).

We describe both the MOIRCS and WIRCam NIR observations along with existing *HST*/ACS data in § 2, the NIR data reduction is discussed in § 3, and the quality of our reduced NIR data is showed in § 4. We also discuss the  $K_s$ -selected catalogs, their number counts and the completeness estimates in § 4. In § 5, we develop and implement  $z_{850}$ -dropout selection criteria to identify LBG candidates at  $z \gtrsim 6.5$  and discuss the implications of our results. We summarize our results in § 6, emphasizing that we combine two NIR surveys of GOODS-N field to construct deep  $K_s$ -band images for this field, needed for a variety of studies.

Throughout this paper we refer to the *HST*/ACS F435W, F606W, F775W, F850LP filters as  $B_{435}$ ,  $V_{606}$ ,  $i_{775}$ ,  $z_{850}$ , and to the *Spitzer*/IRAC 3.6  $\mu$ m, 4.5  $\mu$ m, 5.8  $\mu$ m, 8.0  $\mu$ m filters as [3.6], [4.5], [5.8], [8.0], respectively, for convenience. We assume a *Wilkinson Microwave Anisotropy Probe* (WMAP) cosmology with  $\Omega_m=0.274$ ,  $\Omega_\Lambda=0.726$  and  $H_0=70.5$  km s<sup>-1</sup> Mpc<sup>-1</sup>, in accord with the 5 year WMAP estimates of Komatsu et al. (2009). This corresponds to a look-back time of 12.93 Gyr at  $z \simeq 7$ . Magnitudes are given in the AB system (Oke & Gunn 1983).

## 2. Observations

### 2.1. Subaru/MOIRCS Observations

The MOIRCS is on the Subaru 8.2m telescope, providing wide-field imaging and spectroscopic capability in the NIR bands. In the imaging mode, the MOIRCS provides  $4 \times 7$  arcmin<sup>2</sup> field of view with 0.117'' pixel<sup>-1</sup> using two  $2048 \times 2048$  HgCdTe (HAWAII2) arrays, each of which covers a  $4 \times 3.5$  arcmin<sup>2</sup> field. There is almost no gap between FOVs

of each channel. Details of this instrument are given in Ichikawa et al. (2006). We used the Subaru archive SMOKA<sup>1</sup> to retrieve the MOIRCS observations in the GOODS-N field. Typical exposure time for individual frames varied between  $\sim 50$  to  $\sim 100$  secs and standard nine-point dither patterns (dithering by  $10\text{--}15''$ ) were used (for details see, e.g., Bundy et al. 2009; Kajisawa et al. 2011). These observations were carried out over a period of three years between 2005–2007 (e.g., Wang et al. 2009; Bundy et al. 2009; Kajisawa et al. 2011). They cover an area of about  $109 \text{ arcmin}^2$ , which overlaps with  $\sim 60\%$  of the central region of the GOODS-N ACS field, as shown in Figure 1. The typical seeing for these observations is between  $0.6''$  and  $0.8''$ . Figure 1 shows the GOODS-N ACS field in gray shaded region with black solid line border, and the MOIRCS covered field with dashed black line. The full MOIRCS field is covered by 4 pointings and the field layout is shown by  $2 \times 4$  chips (Figure 1). These observations were done in three broad-band filters  $J$ ,  $H$  and  $K_s$ , whose transmission curves are shown as solid curves in the top panel of the Figure 2.

## 2.2. CFHT/WIRCam Observations

The WIRCam is on the CFHT 3.6m telescope and contains 4  $2048 \times 2048$  pixel HAWAII2-RG detectors, covering a total area of  $20 \times 20 \text{ arcmin}^2$  with a sampling of  $0.3'' \text{ pixel}^{-1}$ . WIRCam is a near-infrared instrument spanning the range  $0.9\text{--}2.4$  microns. Details of this instrument are given in Puget et al. (2004). We used the CFHT archive CADC<sup>2</sup> to retrieve the WIRCam observations in the GOODS-N field. These observations were carried out over a period of three years between 2006–2008 (e.g., Wang et al. 2010). They cover an area of about  $1040 \text{ arcmin}^2$ , and overlap completely with the GOODS-N ACS field as shown by a large dot-dash box in Figure 1. The typical seeing for these observations is between  $0.6''$  and  $0.8''$ . These observations were done in two broad-band filters  $J$  and  $K_s$ , whose transmission curves are shown as dash curves in the top panel of the Figure 2. Table 1 lists relevant information about the NIR data in the GOODS-N field, used in this paper.

Filter transmission curves and total system throughputs used for these observations are shown in Figure 2. WIRCam system throughputs are calculated using their transmission coefficients<sup>3</sup>, and MOIRCS system throughputs are estimated by scaling their transmission curves to the peak throughput given in Table 1 of Ichikawa et al. (2006).

---

<sup>1</sup><http://smoka.nao.ac.jp/>

<sup>2</sup><http://cadwww.dao.nrc.ca/cadc/>

<sup>3</sup><http://www.cfht.hawaii.edu/Instruments/Imaging/WIRCam/WIRCamThroughput.html>

### 2.3. *HST*/ACS Observations

The GOODS-North field was observed with *HST*/ACS broad-band filters  $B_{435}$ ,  $V_{606}$ ,  $i_{775}$ , and  $z_{850}$  (Giavalisco et al. 2004a). The ACS imaging area covers about  $169 \text{ arcmin}^2$  as shown in Figure 1. We used the GOODS team reduction of the ACS images (Giavalisco et al. 2004a). These images have been drizzled from the original ACS pixel scale of  $0.05''$  on to a grid of  $0.03''$  pixels. We used v2.0 of the ACS GOODS images<sup>4</sup> and corresponding AB magnitude zeropoints. The combination of deep *HST*/ACS  $B_{435}$ ,  $V_{606}$ ,  $i_{775}$ ,  $z_{850}$  and ground-based  $J$ ,  $K_s$  observations provide the wavelength coverage needed for selecting LBGs at  $z \gtrsim 6.5$  (Figure 2).

### 3. Near-IR Data Reduction

We have reduced publicly available WIRCam and MOIRCS NIR imaging data in the GOODS-N field by using a reduction pipeline based on the Interactive Data Language (IDL) — Simple Imaging and Mosaicking PipeLineE (**SIMPLE**) developed by Wei-Hao Wang. Details of this pipeline and the steps required to reduce the WIRCam data are given in Wang et al. (2010). We have independently reduced the WIRCam data using this pipeline. Reducing the MOIRCS data is less straightforward and we took the following steps, using the **SIMPLE** software. Many general steps are similar for both datasets.

- **Generate File lists:** We selected all archival observations taken on *photometric nights only*. **SIMPLE** requires input lists of the raw FITS files which are grouped in such a way that each group has same exposure time, is from the same chip, is taken on the same day, and has same coordinates. If a large group of exposures is taken at the same pointing then we break them up into smaller chunks.
- **Reduction:** For the first pass reduction, these file lists are given as input to the main IDL procedure `reduce_moircs.pro` included in the **SIMPLE** software. This script does basic reduction steps including the flat-fielding, cosmic ray removal, sky-subtraction, aligning images, distortion corrections, and general plate solution. It also produces exposure time maps.
- **De-fringing:** The output of the first pass reduction is carefully checked for image defects and/or fringes. The MOIRCS data show strong circular fringes in both chips but more

---

<sup>4</sup><http://archive.stsci.edu/pub/hlsp/goods/v2/>

prominently in chip-2. We use the program `defringe_moircs.pro` provided in the SIMPLE package to remove the fringes. The program first masks detected objects in a flattened and sky-subtracted image and transforms the image to a polar coordinate system, where the circular fringes become nearly straight lines. Then it fits a 5th degree polynomial to each column along the fringes to produce a model fringe image. The fringe model is then transformed back to the original Cartesian coordinate and subtracted from the image. This procedure considerably improves the quality of the reduced images. A very similar fringe removal procedure is adopted by the MOIRCS Deep Survey team (Kajisawa et al. 2011). A few exposures with very bad fringes, which could not be removed through above mentioned process, and/or image defects are not included in the second pass reduction. The reduced images and the exposure time maps are used to form large mosaics.

- **Mosaics:** The final combined mosaic is generated by the procedure `mosaic_wide.pro`. The final MOIRCS images in three filters are registered to each other and to the GOODS ACS images by making the WCS of the MOIRCS images consistent with other multi-wavelength images of the GOODS survey. The final pixel scale for the MOIRCS images is  $0.15'' \text{ pixel}^{-1}$ . For proper comparison with the WIRCam  $0.30'' \text{ pixel}^{-1}$  images, we also generated  $0.30'' \text{ pixel}^{-1}$  MOIRCS images using the IRAF task ‘`blkavg`’.
- **Zeropoints:** The procedure `reduce_std_moircs.pro` was used along with the standard star images from the archive to reduce standard star images and calculate zeropoints in all the three MOIRCS filters ( $J$ ,  $H$ ,  $K_s$ ). The MOIRCS images are in ADU/sec and their derived AB zero-points are 26.175 mag for  $K_s$ , 26.569 mag for  $H$  and 25.965 mag for  $J$  filters. The WIRCam images are in  $\mu\text{Jy}$  units with a zeropoint of 23.9 mag.
- **Combined Images:** We have generated combined (WIRCam and MOIRCS)  $J$ ,  $K_s$  images, which have similar seeing/point spread functions (PSFs), using the Terapix **SWarp** package (Bertin et al. 2002), which resamples and co-adds FITS images using astrometric projection defined in the WCS. The goal of these combined images is to generate the deep  $J$  and  $K_s$ -images in the central  $\sim 60\%$  of the GOODS-N field. The combination was performed as follows: First the images were scaled to a common flux scale. Absolute root mean squared (RMS) noise maps were generated for each mosaic by scaling the mean variance of the images to the mean inverse exposure time maps generated by the SIMPLE reduction package. The data were then combined using a weighted mean combination with the **SWarp** package using the RMS images as the weight image. A bi-linear interpolation kernel was used to re-sample the images onto a common pixel grid. The final combined  $J$ , and  $K_s$  images are in  $\mu\text{Jy}$  units and have a zeropoint of

23.9 mag.

## 4. Near-IR Data Quality and Catalogs

We have reduced archival  $J$ ,  $K_s$ -band WIRCam and MOIRCS images, and shallow  $H$ -band MOIRCS image of the GOODS-N field. We then generated combined images (WIRCam and MOIRCS) in the  $J$  and  $K_s$ -filters, which covers much larger area than the *HST* data. Table 1 shows area coverage information of the NIR data in the GOODS-N field. In this section, we discuss the quality of these combined images, source detections, and the generation of catalogs covering the entire area of this field.

### 4.1. Astrometry

The astrometric solutions of the final mosaiced images were tested by comparing them with the available *HST*/ACS  $z_{850}$ -band catalogs. Figure 3 shows the relative astrometric offsets in RA and DEC between the  $K_s$ -selected and the GOODS-N ACS  $z_{850}$ -selected catalogs. For the purpose of this comparison, we selected well detected/non-saturated compact sources with  $S/N > 20$  and full width half maximum (FWHM)  $< 1.2''$  from the GOODS-N ACS  $z_{850}$ -selected catalog<sup>5</sup> and matched them with the  $K_s$ -selected catalog from the combined image. Figure 3 shows the distribution of the offsets with their mean, median and sigma values. The uncertainty ( $\sigma$ ) in the offsets between the combined  $K_s$ -selected and the ACS  $z_{850}$ -band catalogs is  $0.19''$  for RA (uncertainty in  $RA \cdot \cos(DEC)$  is  $0.09''$ ) and  $0.09''$  for DEC. The uncertainty in the RA is slightly higher than the DEC, but these are still less than one pixel in the  $K_s$ -band ( $0.30'' \text{ pixel}^{-1}$ ). These uncertainties include both the internal errors in the ACS  $z_{850}$ -band catalog and the errors introduced during the image registration of SIMPLE. There are no systematic offsets between the  $K_s$  positions and the ACS  $z_{850}$  catalog.

### 4.2. Photometry

To check the consistency of the photometry in our reduced images, we compared the  $K_s$ -band magnitudes obtained using the **SExtractor** (Bertin & Arnouts 1996) AUTO apertures in the WIRCam image with the MOIRCS image, and also compared  $K_s$ -band magnitudes

---

<sup>5</sup>[http://archive.stsci.edu/pub/hlsp/goods/catalog\\_r2/](http://archive.stsci.edu/pub/hlsp/goods/catalog_r2/)



in the combined image with the  $K_s$ -band magnitudes from the Two Micron All Sky Survey (2MASS). The 2MASS magnitudes have been converted to the AB magnitude system using the conversion given by Ciliegi et al. (2005). The top panel of Figure 4 shows the comparison between the **SExtractor**  $K_s$  magnitudes, for all matched objects, from the WIRCam and the MOIRCS images. There is no significant systematic offset between these two magnitudes, and the mean of their difference is  $\sim 0$  mag, with the uncertainty in the difference being  $\sim 0.30$  mag. The mean value (uncertainty) for  $[K_s(\text{WIRCam}) - K_s(\text{MOIRCS})]$  is 0.03 (0.08) for brighter objects ( $K_s \lesssim 20$  mag). The bottom panel of Figure 4 shows the comparison between the **SExtractor**  $K_s$  magnitudes, measured in the combined images, and the  $K_s$  magnitudes from the 2MASS catalog (Cutri et al. 2003). We compare these magnitudes over the range  $\sim 14$  to  $\sim 16$  mag (as shown by dot-dash vertical lines on the bottom panel of the Figure 4) because of the non-linearity issues in the WIRCam and the selection effects in 2MASS outside this magnitude range (see Wang et al. 2010, for details). The comparison here is based on a small number of bright sources and shows no major systematic offset, with the uncertainty in the difference being very small and mean magnitude difference of 0.02 mag.

### 4.3. Catalogs and Number Counts

We used the **SExtractor** in dual-image mode with the  $K_s$  image as the detection image for  $K_s$ -selected catalog, and  $J$  image for  $J$ -selected catalog. We generated the RMS maps from the weight/exposure time maps and used them during the **SExtractor** runs to get a better estimate of the photometric errors, and hence, of the  $S/N$ . Here,  $S/N$  is defined as 1.0857 divided by the **SExtractor** error in the total magnitude, which is similar to FLUX\_AUTO/FLUXERR\_AUTO. These RMS maps also help to exclude false and spurious detections at the edges with low signal-to-noise values. We set the DEBLEND\_MINCONT parameter to 0.0001, DETECT\_MINAREA to 4 pixels (2 pixels for  $J$ -selected catalog) and detection threshold to  $2.0\sigma$  ( $1\sigma$  for  $J$ -selected), and used convolution with a 3 pixel Gaussian filter in the **SExtractor** configuration file. Table 2 lists the **SExtractor** parameters used to generate  $K_s$  and  $J$ -band selected catalogs in the GOODS-N field. We used **SExtractor** MAG\_AUTO as a measure of the total magnitude. The left 4-panels in Figure 5 show the source counts (i.e., number per arcmin<sup>2</sup> per 0.5 mag bin) in  $K_s$  and  $J$  bands. The leftmost two panels show the MOIRCS and WIRCam  $K_s$ -band counts. They both reach comparable depths marked by dashed vertical lines. The right panels show the  $K_s$ - and  $J$ -band number counts obtained from the combined image. Because of the non-uniform exposure time in the WIRCam and MOIRCS images, the combined  $K_s$ -band image is  $\sim 0.3$ – $0.5$  mag deeper than either WIRCam or MOIRCS image.

We quantify the depth and completeness in our  $K_s$ - and  $J$ -band images by inserting numerous fake sources of varying magnitudes into the reduced images and recovering them using the same **SExtractor** parameters (Table 2) used for the real sources. Fake sources were given Gaussian profiles with the FWHM values similar to the point sources in our image. We define the image depth by the magnitude corresponding to a recovery rate of 50%. This depth implies a slightly lower detection rate for real galaxies, which are more extended. The rightmost two panels in Figure 5 show the  $3\sigma$  completeness curves (dashed curves) for both images. The top panel shows completeness for  $K_s$ -band image, while the bottom panel is for the  $J$ -band. The dashed vertical line in each panel shows the magnitude at which the number counts fall to 50% of their peak value, which we consider as a measure of the completeness limit for these images.

We also quantify reliability of our catalogs by doing the negative image test. We multiply the science (positive) image by  $-1$  to get a negative image. We then apply same detection procedure using **SExtractor** parameters listed in Table 2. The number of detected ‘objects’ in these negative images quantify reliability of these catalogs. The dot-dash curve in the rightmost two panels of Figure 5 shows the reliability curve for both  $J$ - and  $K_s$ -selected catalogs. The dot-dash vertical line shows the magnitude at which the reliability falls to 50%.

The simulations and the observed number counts show that both ( $J$  and  $K_s$ ) combined images are complete to AB magnitude limit of  $\sim 25$  mag ( $3\sigma$ ), and 50% reliable to  $\sim 24.5$  mag. We also have  $H$ -band data in the GOODS-N region from the Subaru telescope observations. The  $H$ -band MOIRCS image is shallower compared to  $J$  or  $K_s$ -bands by  $\sim 1$  mag, but can be very useful for brighter objects in this field.

## 5. Lyman Break Galaxies at $z \gtrsim 6.5$ ( $z_{850}$ -dropouts)

As an application of these NIR data in the GOODS-N field, we combine these with the existing *HST*/ACS data to look for  $z_{850}$ -dropout galaxies, which are LBG candidates at  $z \gtrsim 6.5$ . To identify  $z_{850}$ -dropouts, we search for Lyman-break signature that occurs at the rest-frame 1216 Å (Madau 1995) using the dropout technique. This technique is based on photometric color selection and requires imaging in at least two filters, one to the blue side of the break and the other to the red side (usually we have two or more filters on both sides). The presence of Lyman break makes high-redshift galaxies much fainter in the blue band than in the red one, or in other words, it makes them appear to “drop-out” from the blue band. For this reason, this method is also known as the dropout selection, and the candidates found in this way are generally referred to as “dropouts”. At  $z \gtrsim 6.5$ , this

break moves through observed  $z_{850}$ -band ( $\sim 9100 \text{ \AA}$ ). Figure 2 shows the locations of the rest-frame  $1216 \text{ \AA}$  Lyman break at  $z \gtrsim 6.5$ . It is clear that ground-based  $J$  and  $K_s$  band filters, combined with the ACS bands are crucial in identifying LBG candidates at  $z \gtrsim 6.5$ .

The drizzled ACS images in  $B_{435}$ ,  $V_{606}$ ,  $i_{775}$ ,  $z_{850}$  filters have a spatial resolution of  $0.03''$  pixel $^{-1}$ , compared to combined  $J$  and  $K_s$ -band images which have  $0.30''$  pixel $^{-1}$  resolution. Therefore, to perform matched aperture photometry, we generated re-binned ( $10 \times 10$ ), PSF matched, ACS images to properly compare with combined  $J$  and  $K_s$ -band images. Details of catalog generation, completeness, and reliability are discussed in § 4.3. In summary, we performed matched-aperture photometry on  $B_{435}$ ,  $V_{606}$ ,  $i_{775}$ ,  $z_{850}$ ,  $J$ ,  $K_s$  images by running the **SExtractor** in the dual-image mode with  $J$ -band as the detection image. We used corresponding RMS maps to reduce the number of spurious sources detected in the low signal-to-noise ratio edge of the images. For object identification, we adopted a limit of at least 2 contiguous pixels above a threshold of  $1\sigma$ . We constructed a  $J$ -selected catalog using **SExtractor** parameters shown in Table 2. We used **SExtractor** MAG\_AUTO, with the default Kron factor=2.5 and minimum radius=3.5, as a measure of the total magnitude. This catalog was used to select LBG candidates at  $z \gtrsim 6.5$  based on the dropout color selection criteria. The colors of the objects were estimated from the matched-aperture MAG\_AUTO photometry on the *HST*/ACS and combined NIR images, as discussed above.

## 5.1. $z_{850}$ -dropout Selection

### 5.1.1. Color Selection

The  $z_{850}$ -dropout selection uses color criteria obtained from the stellar population models of Bruzual & Charlot (2003, BC03). Figure 6 (top panel) shows the BC03 star-forming galaxy models with  $E(B-V)=0, 0.15, 0.30$  mag (solid blue lines with open circles showing different redshifts), expected colors of late-type stars (black filled circles) from Pickles (1998), and tracks of lower-redshift ellipticals (red lines) from three different models (BC03, Kinney et al. 1996; Coleman et al. 1980). Our selection region is shown as a gray shaded area. We have corrected the colors for IGM attenuation using the prescription of Madau (1995). The two-color dropout selection criteria adopted here are similar to those used to identify and study LBG candidates at  $z \simeq 1-8$  (e.g., Giavalisco et al. 2004b; Bouwens et al. 2008; Hathi et al. 2008; Yan et al. 2010; Hathi et al. 2010). The  $J$ -selected catalog is used to select  $z_{850}$ -dropouts from the  $(z_{850} - J)$  vs.  $(J - K_s)$  color-color diagram (Figure 6) using

the following criteria:

$$\left\{ \begin{array}{l} (z_{850} - J) > 1.5 \text{ mag} \\ \text{and } (J - K_s) < 1.2 \text{ mag} \\ \text{and } (z_{850} - J) > 0.99 + [0.85 \times (J - K_s)] \text{ mag} \\ \text{and } (J - K_s) > -0.5 \text{ mag} \\ \text{and } S/N(J) \geq 2.0 \end{array} \right.$$

We also require non-detection of the candidates ( $S/N \lesssim 1$ ) in ACS optical  $B_{435}$ ,  $V_{606}$ ,  $i_{775}$ -bands. The  $S/N$  cut in the  $J$ -band ( $\geq 2$ ) corresponds to an AB magnitude limit of  $\sim 25.3$  mag. We have also applied the additional criterion  $(J - K_s) > -0.5$  mag to eliminate the possibility of selecting spurious candidates (e.g., extreme equivalent width objects at lower redshifts: van der Wel et al. 2011; Atek et al. 2011), since this color-color space is based only on  $z_{850}$ ,  $J$ , and  $K_s$  filters, and it is required that LBG candidates be detected and are relatively bright in the  $K_s$ -band. After initial color and  $S/N$  cuts, we visually inspected each selected object to remove any spurious source (due to image defects or their proximity to a bright foreground object, edge effects, or faint stellar diffraction spike). This leaves 14 potential candidates as shown in the top panel of the Figure 6.

### 5.1.2. Redshift Selection Functions

To generate redshift selection functions, we ran simulations to calculate  $P(m, z)$ , which is the probability that a galaxy with apparent magnitude  $m$  at redshift  $z$  will be detected in the image *and* will meet our color selection criteria (§ 5.1.1). In these simulations, large numbers of artificial objects with a range of redshifts and magnitudes were added to real images, and then recovered using exactly the same method and selection criteria that were employed for the real observations. We simulated these objects in four *HST*/ACS,  $J$ , and  $K_s$  bands because we use these filters to perform dropout color selection as shown in § 5.1.1. The input spectrum for each simulated object is from BC03 models with constant star-formation history, three different E(B–V) values, two different metallicities, and applying Madau (1995) prescription for IGM attenuation below rest 1216 Å. The bottom panel of the Figure 6 shows the redshift selection function for different  $J$  magnitudes.

### 5.1.3. Spitzer/IRAC Colors

The GOODS-N field has deep *Spitzer*/IRAC imaging in [3.6], [4.5], [5.8], and [8.0] channels. These observations are vital in assessing the reliability of our  $z_{850}$ -dropout candidates.

The  $(J - [3.6])$  and  $(J - [4.5])$  colors are used to differentiate between extremely red objects (EROs; Yan et al. 2004) at  $z \simeq 2$  and high redshift candidates. The EROs have  $(J - [3.6])$  and  $(J - [4.5])$  colors in excess of  $\sim 2.5$  (Yan et al. 2004), putting a constraint on the colors of high redshift galaxy candidates to have bluer colors (e.g., Eyles et al. 2007). To examine this, we used *Spitzer*/IRAC [3.6] and [4.5] images to estimate magnitudes of 14 candidates in these bands. We simply calculated IRAC total magnitudes from  $3''$ -diameter aperture magnitudes and used aperture corrections given by Yan et al. (2005). To confirm our photometry across different NIR passbands, we compared our **SExtractor** magnitudes with the Template FITting (TFIT; Laidler et al. 2007) magnitudes. The TFIT technique performs consistent multi-waveband photometry on images with widely different resolutions. Our  $J$ ,  $K_s$ , [3.6], and [4.5] **SExtractor** magnitudes are very similar (within uncertainties) to the TFIT magnitudes obtained using different set of proprietary CFHT NIR images in this region. To confirm our color selection and to differentiate between LBG candidates at  $z \gtrsim 6.5$  and EROs at  $z \simeq 2$ , we estimated photometric redshifts for 14 candidates.

We used three different codes to estimate photometric redshifts, namely **HyperZ** (Bolzonella et al. 2000), **EAZY** (Brammer et al. 2008), and **Le PHARE**<sup>6</sup> (Arnouts et al. 1999; Ilbert et al. 2006). Out of 14 candidates, the photometric redshift estimate for 12 objects was not consistent between three codes with few objects showing possible detection in optical bands during visual inspection. Therefore, we find two possible LBG candidates at  $z \gtrsim 6.5$  after applying our color criteria, visually confirming non-detections in optical bands, and based on our photometric redshift estimates. These two candidates are shown in Figure 7. Table 3 lists the coordinates and TFIT photometry of these candidates. Their spectral energy distributions and best-fit models based on **Le PHARE** code are shown in Figure 8. Though photometric redshifts show high probability that these are LBG candidates at  $z \gtrsim 6.5$ , the exact nature of these LBG candidates is unclear, and we will explore their properties and few possible scenarios.

## 5.2. Are these luminous objects at $z \gtrsim 6.5$ ?

Based on the photometric data, it is unclear whether the objects found here are genuinely at  $z \gtrsim 6.5$  or not. Both objects meet the color selections suggested by previous studies (e.g., Bouwens et al. 2008; Capak et al. 2011), but they are very bright ( $J \lesssim 24$  mag) to be at this redshift, specially in a comparatively smaller area ( $\sim 169$  arcmin<sup>2</sup>) of the GOODS-N field. In this section, we discuss properties of these candidates.

---

<sup>6</sup><http://www.cfht.hawaii.edu/~arnouts/LEPHARE/lephare.html>

### 5.2.1. Morphologies

The GOODS-N catalog of  $i_{775}$ -band dropouts<sup>7</sup> selected using criteria outlined in Beckwith et al. (2006) includes these two candidates, but this catalog is only based on  $HST/ACS$   $B_{435}$ ,  $V_{606}$ ,  $i_{775}$ ,  $z_{850}$  magnitudes. Addition of  $J$  and  $K_s$  observations help to distinguish between an object at  $z \simeq 6$  and  $z \gtrsim 6.5$ , depending on the location of Lyman break in the  $z_{850}$ -band. Both these candidates are very faint but compact in  $z_{850}$ -band (stellarity  $> 0.5$ ) so there is a strong possibility that these objects are faint point sources (late-type stars). The  $J$ -band **SExtractor** stellarity for candidate A is 0.54, while it is 0.13 for candidate B, but the  $J$ -band PSF is less sharper than ACS so  $J$ -band stellarity could be a less convincing measure of compactness for these objects. Therefore, based on  $z_{850}$ -band compactness measurements, it is possible that these  $z_{850}$ -dropout candidates could be stellar-like.

### 5.2.2. Passive Galaxies

One of the major interlopers in selecting high redshift dropout galaxies is the lower redshift passively evolving galaxies. The 4000 Å Balmer break in old galaxies at  $z \simeq 2$  could potentially be mistaken for a Lyman break at  $z \gtrsim 6.5$ . These passive galaxies can be modelled with suitable set of spectral synthesis models. We use the BC03 models to predict the colors of such objects. Figure 6 (top panel) shows predicted colors of these old galaxies as a function of redshift through various evolutionary tracks plotted in red. The color selection region of  $z_{850}$ -dropouts (gray shaded region in the top panel of Figure 6) based on  $(z_{850} - J)$  and  $(J - K_s)$  avoids these tracks, and hence, minimizes contamination of our sample by these passive galaxies. Also, the EROs at  $z \simeq 2$  have very red  $(J - [3.6])$  and  $(J - [4.5])$  colors in excess of  $\sim 2.5$  (Yan et al. 2004) while our  $z_{850}$ -dropout candidates have much bluer NIR colors, which also suggests that these candidates are not likely EROs at  $z \simeq 2$ .

### 5.2.3. Late-type Stars

The NIR colors of Galactic cool stars are also very similar to the high redshift dropout candidates and can mimic the Lyman break in the color-color space as they are also optically faint and bright in the NIR. The main distinguishing properties between a high redshift galaxy candidate and a cool dwarf are their morphologies and NIR colors. We discussed morphologies in § 5.2.1. Here, we investigate the  $J$ ,  $K_s$  and *Spitzer*/IRAC colors which will

---

<sup>7</sup><http://archive.stsci.edu/pub/hlsp/dropouts/>

shed light on the nature of these  $z_{850}$ -dropout candidates. The  $(z_{850} - J)$  and  $(J - K_s)$  colors in Figure 6 show expected colors of late-type stars (black filled circles) based on Pickles (1998) models. The colors of candidate B fall in the region occupied by the cool dwarfs, while candidate A has redder  $(J - K_s)$  color. Therefore, based on these colors, it is possible that candidate B could be a late-type star.

Stanway et al. (2008) have proposed  $J$ ,  $K_s$  and *Spitzer*/IRAC color cuts, which were designed to remove passive galaxies at  $z \lesssim 2$  and late-type stars. The  $z_{850}$ -dropout candidate A successfully passes these four color criteria, while candidate B does not pass the  $([3.6] - [4.5])$  color cut. These criteria also indicate that the candidate B could be an interloper (most likely a late-type star) based on these NIR colors.

#### 5.2.4. Photometric Redshifts

Kajisawa et al. (2011) have analysed MOIRCS data, separating it into two regions — the deep and the wide. Our  $z_{850}$ -dropout candidates are not located in the deep MOIRCS region, but are covered by the shallower wide region. Kajisawa et al. (2011) estimated photometric redshifts of these candidates using their own MOIRCS wide photometric catalog. They measured photometric redshift using four different techniques. Three out of four techniques estimate redshift of these candidates to be at  $z \gtrsim 6.5$ , while the fourth approach (using EAZY code) estimates lower redshift ( $z \simeq 2$ ) for these candidates.

We performed SED fitting using available multi-wavelength data (optical to NIR) in the GOODS-N field to predict photometric redshifts of our  $z_{850}$ -dropout candidates. We used three photometric redshift codes (**Le PHARE**, **HyperZ** and **EAZY**) on TFIT photometry to estimate their redshifts. The TFIT photometry generates accurate photometric redshifts, as shown by Dahlen et al. (2010) for the GOODS-S field. These codes predict high probability for these two candidates to be at  $z \gtrsim 6.5$ . Figure 8 shows SED fitting using **Le PHARE** code for two types of templates — blue for a late-type star (from Chabrier et al. 2000 library) and red for a star forming galaxy (from BC03 library) at  $z \gtrsim 6.5$ . The SED fitting for candidate B shows equal probability (very similar  $\chi^2$ ) for both these templates, while candidate A has a higher probability for a LBG at  $z \gtrsim 6.5$ . This implies that candidate B could be a late-type star, but it is also equally likely to be a high redshift galaxy. We also note that due to lack of Y-band data, the exact location of the Lyman break between the  $z_{850}$ - and  $J$ -band could be somewhat uncertain, and that would increase the uncertainty in the photometric redshift.

### 5.2.5. Keck Spectroscopy

We used the DEep Imaging Multi-Object Spectrograph (DEIMOS; Faber et al. 2003) on the 10m Keck telescope to perform spectroscopic observations of these two candidates during our March–April 2011 observing run. The total exposure time for these observations was  $\sim 4$  hours. The seeing was in the range of  $0.5'' - 0.7''$ . We used the GC455 filter and the 600 line  $\text{mm}^{-1}$  grating, blazed at  $7400 \text{ \AA}$ . The spectral coverage was between  $\sim 5500 \text{ \AA}$  and  $\sim 10000 \text{ \AA}$ . The spatial pixel scale was  $0.1185'' \text{ pix}^{-1}$ , and the spectral dispersion was  $0.65 \text{ \AA pix}^{-1}$ . The slit widths were  $1''$ . The preliminary reduction were performed using the `spec2d` IDL pipeline<sup>8</sup> developed by the DEEP2 Team (Cooper et al. 2012; Newman et al. 2012). Wavelength calibration was performed by fitting to the arc lamp emission lines. The standard stars and science targets were observed using the same slit width so we did not apply any corrections due to slit-loss effects.

We present the Keck spectrum of one  $z_{850}$ -dropout candidate which has high enough  $S/N$  ratio to make a redshift measurement possible. For the second candidate, because of the unfortunate location on the mask and sky lines, the spectrum is not reliable. In Figure 9, we show one and two dimensional DEIMOS spectra of the  $z_{850}$ -dropout candidate B between 8400 and 10000  $\text{\AA}$ . Figure 9 shows a weak emission line at  $\sim 9090 \text{ \AA}$  indicated by a dot-dash line in the one dimensional spectrum, and by a red arrow in the two dimensional stamp. The sky spectrum is shown at the bottom of the one dimensional spectrum and there is no major sky line at this wavelength. This spectral feature also shows asymmetric nature of a  $\text{Ly}\alpha$  line, and we don't see any clear detection of other lines, so we tentatively identify this line as a  $\text{Ly}\alpha$  at  $z \simeq 6.5$ . The estimated line flux is  $\sim 1.4 \times 10^{-17} \text{ erg s}^{-1} \text{ cm}^{-2}$ , and the rest-frame equivalent width (EW) is  $\gtrsim 21 \text{ \AA}$ . Hence, candidate B is a possible LBG at  $z \simeq 6.5$ , consistent with its photometric redshift. The red part of the spectrum of candidate A is mostly affected by improper masking and sky lines, so it is unreliable and inconclusive. The bluer part of the spectrum (below 8000  $\text{\AA}$ ) does not show any clear detection of emission line. This could imply that candidate A is not a low redshift galaxy, but does not rule out other possibilities (e.g., late-type star or LBG). This spectrum cannot conclusively predict the nature of candidate A — whose photometric redshift is  $\sim 7.4$  — because the possible  $\text{Ly}\alpha$  emission line would be around 10200  $\text{\AA}$ , which we cannot identify. Therefore, the Keck spectrum of candidate A cannot differentiate between a late-type star or a LBG at  $z \gtrsim 6.5$ . We will try to re-observe these candidates with Keck/DEIMOS or MOSFIRE NIR spectroscopy.

The three spectroscopically confirmed objects of Ono et al. (2012) at  $z \gtrsim 6.5$  were also

---

<sup>8</sup><http://astro.berkeley.edu/~cooper/deep/spec2d/>



observed during the same Keck observing run. These objects were about 1 mag fainter in the continuum than our candidates, and all three showed detectable Ly $\alpha$  in emission. These successful Ly $\alpha$  detections along with the likely Ly $\alpha$  detection in Candidate B allow us to put lower limits on Ly $\alpha$  line emission from our  $z_{850}$ -dropout candidate A. The three Ono et al. (2012) objects have Ly $\alpha$  flux limits ( $1\sigma$ ) in range of  $2.5\text{--}2.7 \times 10^{-17}$  erg s $^{-1}$  cm $^{-2}$ , and rest-frame EW between 33 and 43 Å. These flux and EW measurements are consistent with other confirmed Ly $\alpha$  emitters at  $z \gtrsim 6.5$  (e.g., Vanzella et al. 2011; Pentericci et al. 2011). This implies that if our candidate A is a Ly $\alpha$  emitter, then we could detect Ly $\alpha$  line with flux  $\gtrsim 1.4 \times 10^{-17}$  erg s $^{-1}$  cm $^{-2}$ , and EW  $\gtrsim 20$  Å.

The fraction of LBGs showing Ly $\alpha$  in emission is a strong function of the absolute UV-magnitude ( $M_{\text{UV}}$ ), i.e., fraction increases for fainter galaxies. This has been confirmed by observations at  $z \simeq 6\text{--}8$  (e.g., Stark et al. 2011; Schenker et al. 2012), and also by smoothed particle hydrodynamics simulations (e.g., Forero-Romero et al. 2012). These studies imply that more luminous LBGs are less likely to show Ly $\alpha$  in emission, and it is possible that candidate A will not show Ly $\alpha$  line because of its luminosity. We should also emphasize that, at similar continuum magnitudes, Capak et al. (2011) could not clearly detect Ly $\alpha$  emission for their LBG candidates at  $z \gtrsim 6.5$ . Therefore, to clearly identify the nature of our LBG candidates at  $z \gtrsim 6.5$ , we need deep NIR spectroscopy from Keck/MOSFIRE or *HST*/WFC3.

In this section, we investigated morphology, NIR/IRAC colors, and Keck spectroscopy of our two  $z_{850}$ -dropout candidates. We find that though photometric redshift and NIR colors of candidate A support that it could be a LBG at  $z \simeq 7$ , because of inconclusive Keck spectrum the true nature of this candidate is uncertain. The candidate B could be a real  $z_{850}$ -dropout galaxy at  $z \simeq 6.5$  based on a weak Ly $\alpha$  detection in the Keck spectrum, but we cannot rule out other possibilities based on our data. Therefore, it is plausible that one or none of these candidates are at  $z \gtrsim 6.5$ . Hence, we conclude that we find  $1 \pm 1$  LBG candidates at  $z \gtrsim 6.5$ , brighter than  $AB \sim 24.5$  mag, in the GOODS-N field.

### 5.3. Discussion

#### 5.3.1. Other Surveys and Cosmic Variance

The rarity of bright LBG candidates at  $z \gtrsim 6.5$  in a comparatively smaller area ( $\sim 169$  arcmin $^2$ ) questions as why other surveys have not found such objects. Conselice et al. (2011) used 30 NICMOS pointings of massive galaxies at  $z \simeq 1.7\text{--}2.9$  to cover smaller area of the GOODS-N field with NIR data. These NICMOS observations were used by

Bouwens et al. (2010b) to search for LBGs at  $z \gtrsim 6.5$ , but they do not cover the area in which we find our two candidates. The PEARS grism survey (Malhotra 2007) in this field also does not cover this region, which could have helped to confirm the nature of our  $z_{850}$ -dropout candidates.

Ouchi et al. (2009) survey was a  $Y$ -band survey in the GOODS-N field and does not use the NIR bands. This survey requires a detection brighter than 26 mag in the  $Y$ -band ( $\sim 1$  micron). Their redshift selection function shows a survey optimized to select galaxy candidates at  $6.5 < z < 7.1$ , therefore if our candidates are outside this redshift range then Ouchi et al. (2009) could not have found them. Moreover, they used Suprime-Cam on the Subaru Telescope to do a wide-area survey at 1 micron, which is not possible in the NIR simply because of the small field of view of NIR detectors. As a result, they also surveyed the extended GOODS-N region with no *HST* data. In the present study, we have generated deep NIR images in the GOODS-N area for which we have very deep *HST*/ACS and *Spitzer*/IRAC data, all with consistent photometry using TFIT technique. Combining these data with the NIR data, we can then search for the  $z_{850}$ -band dropout galaxies, which puts limits on the source density of these sources. Also, the availability of combined  $K_s$ -band data allows searches for high- $z$  galaxies when *HST*/WFC3 ( $YJH$ ) data become available through the CANDELS (Grogin et al. 2011; Koekemoer et al. 2011).

Similar wide area NIR surveys have been done in the GOODS-S and other fields to look for brighter LBG candidates at  $z \gtrsim 6.5$ . Hickey et al. (2010) used ESO/VLT observations in the GOODS-S field covering  $\sim 119$  arcmin<sup>2</sup> to search for high redshift LBGs. They found four possible candidates at  $z \gtrsim 6.5$  with an AB magnitude brighter than 25.5 mag. Hickey et al. (2010) survey covers slightly smaller area than our survey and does not find any  $z_{850}$ -dropouts with  $J$  magnitude brighter than 24 mag, but they do find objects with similar  $K_s$  magnitudes as our candidates. Castellano et al. (2010) also conducted a VLT survey covering three different fields (total area 161 arcmin<sup>2</sup>) to search for LBGs at  $z \gtrsim 6.5$ . They found a total of 15 candidates but all are fainter than 25.5 mag. The *HST*/WFC3 parallel imaging surveys (Yan et al. 2011; Trenti et al. 2011) have covered  $\sim 125$  arcmin<sup>2</sup> area — which is smaller than our current survey area — to search for  $Y_{098}$ -dropouts, which is optimized to identify LBGs at  $z \gtrsim 7.5$ . These surveys have identified few candidates with AB magnitude fainter than or equal to 25 mag. Though most of the surveys have smaller area coverage than our full area GOODS-N field ( $\sim 169$  arcmin<sup>2</sup>), they don't find any LBG candidates at  $z \gtrsim 6.5$  with magnitudes brighter than  $J_{AB} \sim 24.5$  mag.

Stanway et al. (2008) performed extensive search for LBGs at  $z \gtrsim 6.5$  in 10 widely separated fields as a part of the ESO Remote Galaxy Survey (ERGS). This survey covered  $\sim 225$  arcmin<sup>2</sup> and found one possible LBG candidate at  $z \gtrsim 6.5$  with  $J_{AB} \sim 23.6$  mag, which

is very similar to  $J$  magnitude of our  $z_{850}$ -dropout candidates. If Stanway et al. (2008) bright candidate is confirmed, then the surface density of such bright LBG candidates at  $z \gtrsim 6.5$  is  $\sim 0.4 \times 10^{-2}$  per arcmin<sup>2</sup> in the ERGS.

Based on other wide area surveys, it seems very unlikely that both of our bright candidates are truly at  $z \gtrsim 6.5$ . The GOODS-N field is a comparatively small area to find two such bright LBG candidates at such a high redshift. Capak et al. (2011) found three possible  $z_{850}$ -dropout candidates with similar brightnesses, but in a area as large as 2 deg<sup>2</sup>. That being said, if one of our candidates is confirmed to be at  $z \gtrsim 6.5$  then the estimated surface density is  $\sim 0.5 \times 10^{-2}$  per arcmin<sup>2</sup>, which is very similar to what Stanway et al. (2008) found in the ERGS. Therefore, finding such a bright LBG candidate at  $z \gtrsim 6.5$  in a survey area of  $\sim 169$  arcmin<sup>2</sup> is a statistical possibility based on cosmic variance.

### 5.3.2. Implications

We find two possible LBG candidates at  $z \gtrsim 6.5$  from our analysis of NIR images in the GOODS-N field ( $\sim 169$  arcmin<sup>2</sup>). The first candidate could be a real LBG at  $z \simeq 6.5$  based on a possible Ly $\alpha$  line in the Keck spectrum, and the photometric redshift of the second candidate support its high redshift nature. If confirmed, these are among the brightest LBG candidates at  $z \gtrsim 6.5$ . At a redshift of  $z \simeq 7$ , we estimate absolute magnitudes  $M_{UV} \simeq -23.7$  and  $-23.1$  mag for candidates A and B, respectively, which is  $\sim 1$  mag brighter than spectroscopically confirmed Ly $\alpha$  emitting  $z_{850}$ -dropouts by Ono et al. (2012). The two possible LBG candidates at  $z \gtrsim 6.5$  in the GOODS-N field implies a surface density of  $\sim 1.0 \times 10^{-2}$  per arcmin<sup>2</sup> at  $J < 24.5$  mag. This is consistent with other surveys (e.g., Stanway et al. 2008; Ouchi et al. 2009; Yan et al. 2011) focusing on galaxies brighter than 25.5 mag.

Using Madau et al. (1998) formalism, the rest-frame UV luminosities of our candidates correspond to star formation rates (SFRs) of  $\sim 100$ – $200$  M $_{\odot}$  yr<sup>-1</sup>. As a rough estimate, if they keep forming stars at the same rates to  $z \sim 5$ , they could accumulate stellar masses of  $(0.5$ – $1.0) \times 10^{11}$  M $_{\odot}$  in next  $\sim 400$  million years. Therefore, our luminous  $z_{850}$ -dropout candidates could be progenitors of massive LBGs ( $\sim 10^{11}$  M $_{\odot}$ ) observed at  $z \sim 5$  (e.g., Wiklind et al. 2008).

The bright-end of the luminosity function declines exponentially so we expect fewer bright galaxies at these redshifts. The surface density, which we predict based on our luminous LBG candidates at  $z \gtrsim 6.5$ , is significantly higher than what is expected from smaller area fainter *HST* surveys, but such a difference at the bright end of the luminosity function is not surprising and is within the theoretical limits based on halo mass function (Bouwens et al.

2008; Capak et al. 2011). The star formation processes are not well understood at these redshifts, so it is very likely that the mechanism involving truncation of star formation and feedback are different at higher redshifts and this can lead to a flatter bright-end for the luminosity function.

To estimate the number density of these possible bright  $z_{850}$ -dropouts, the GOODS-N volume was estimated using  $P(m, z)$  simulations (details in § 5.1.3). This volume estimate is very similar to the estimate obtained using cosmic variance calculator of Trenti & Stiavelli (2008). The number density for one object at  $z \gtrsim 6.5$  obtained using this volume is plotted in Figure 10 along with other number densities from the literature (Bouwens et al. 2008; Oesch et al. 2009, 2010; Capak et al. 2011; Bowler et al. 2012). The number densities at  $M_{UV} \simeq -23.5$  mag, if confirmed, point to a ‘no-knee’ type luminosity function at  $z \gtrsim 6.5$ , which has been considered as a possibility for  $z > 6$  luminosity functions (e.g., Bouwens et al. 2008; Capak et al. 2011). The bright-end of the luminosity function cannot be constrained by faint, small area surveys. To find brightest galaxies and get better constraints for the bright-end of the LF at these redshifts we will need wide area, shallow surveys (e.g., Trenti et al. 2011; Yan et al. 2011; Grogin et al. 2011). Though these bright objects are luminous, it is still difficult to get spectroscopic confirmations — even with 10m Keck telescope (as discussed in § 5.2.5) — if they are not strong Ly- $\alpha$  emitters (also see Capak et al. 2011). The high resolution *HST* imaging in NIR with the CANDELS and deep WFC3/IR grism observations (e.g., Brammer et al. 2012) may help to confirm these and other such candidates.

## 6. Summary

We have combined archival NIR images obtained from the Subaru and the CFHT telescopes to generate deep  $J$  and  $K_s$  band images in the GOODS-N field. These NIR data are vital for variety of multi-wavelength science goals. We use these images to search for bright  $z_{850}$ -dropouts, (i.e., LBG candidates at  $z \gtrsim 6.5$ ). We find two likely candidates at  $z \gtrsim 6.5$ . We attempted Keck/DEIMOS spectroscopy to identify true nature of these candidates. One candidate has a weak spectral feature which we tentatively identify as Ly $\alpha$  at  $z \simeq 6.5$ . Though the colors and photometric redshifts of the second candidate indicate that it is likely to be at  $z \gtrsim 6.5$ , the true nature of this candidate is ambiguous. Hence, based on our analysis, we predict  $1 \pm 1$  LBG candidates at  $z \gtrsim 6.5$ , brighter than AB  $\sim 24.5$  mag, in the GOODS-N field. The expected SFRs of 100–200  $M_\odot \text{ yr}^{-1}$  implies that these LBG candidates at  $z \gtrsim 6.5$  are likely to be the progenitors of massive LBGs found at  $z \simeq 5$ . The number density of such luminous LBGs puts strong constraints on the bright-end of the luminosity function at  $z \gtrsim 6.5$ , consistent within the theoretical limit based on the halo mass

function. Deep NIR spectroscopic observations will help to confirm these bright candidates as well as shed light on the nature of such luminous LBGs at  $z \gtrsim 6.5$ .

We thank the referee for helpful comments and suggestions that significantly improved this paper. We acknowledge valuable comments and suggestions from Mark Dickinson. We are grateful to Kyle Penner and Shoubaneh Hemmati for their help in reducing the Keck spectroscopy data. NPH acknowledges support provided by NASA through grants HST-GO-11702.02-A and HST-GO-11359.08-A from the Space Telescope Science Institute, which is operated by AURA, Inc., under NASA contract NAS 5-26555.

## REFERENCES

- Arnouts, S., et al. 1999, MNRAS, 310, 540
- Atek, H., et al. 2011, ApJ, 743, 121
- Beckwith, S., et al. 2006, AJ, 132, 1729
- Bertin, E., & Arnouts, S. 1996, A&AS, 117, 393
- Bertin, E., Mellier, Y., Radovich, M., Missonnier, G., Didelon, P., & Morin, B. 2002, *Astronomical Data Analysis Software and Systems XI* (Proc. ASP Conf. Ser. 281), ed. D. A. Bohlender, D. Durand, & T. H. Handley (San Francisco, CA: ASP), 228
- Bolzonella, M., Miralles, J. M., & Pelló, R. 2000, A&A, 363, 476
- Bouwens, R. J., Illingworth, G. D., Franx, M., & Ford, H. 2008, ApJ, 686, 230
- Bouwens, R. J., et al. 2010a, ApJ, 709, L133
- Bouwens, R. J., et al. 2010b, ApJ, 725, 1587
- Bowler, R. A. A., Dunlop, J. S., McLure, R. J., et al. 2012, MNRAS, submitted (arXiv:1205.4270)
- Bradley, L. D., et al. 2012, ApJ, 747, 3
- Brammer, G. B., van Dokkum, P. G., & Coppi, P. 2008, ApJ, 686, 1503
- Brammer, G. B., van Dokkum, P. G., Franx, M., et al. 2012, ApJS, 200, 13
- Bruzual, G., & Charlot, S. 2003, MNRAS, 344, 1000

- Bundy, K., Fukugita, M., Ellis, R. S., Targett, T. A., Belli, S., & Kodama, T. 2009, *ApJ*, 697, 1369
- Capak, P., et al. 2011, *ApJ*, 730, 68
- Castellano, M., et al. 2010, *A&A*, 524, 28
- Chabrier, G., Baraffee, I., Allard, F., & Hauschildt, P. 2000, *ApJ*, 542, 464
- Ciliegi, P., et al. 2005, *A&A*, 441, 879
- Coleman, G. D., Wu, C.-C., & Weedman, D. W. 1980, *ApJS*, 43, 393
- Conselice, C. J., et al. 2011, *MNRAS*, 413, 80
- Cooper, M. C., Newman, J. A., Davis, M., et al. 2012, *Astrophysics Source Code Library*, record ascl:1203.003, 3003
- Cutri, R. M., et al. 2003, *The IRSA 2MASS All-Sky Point Source Catalog*, NASA/IPAC Infrared Science Archive (<http://irsa.ipac.caltech.edu/applications/Gator/>)
- Dahlen, T., et al. 2010, *ApJ*, 724, 425
- Eyles, L. P., Bunker, A. J., Ellis, R. S., Lacy, M., Stanway, E. R., Stark, D. P., & Chiu, K. 2007, *MNRAS*, 374, 910
- Faber, S. M., et al. 2003, *SPIE*, 4841, 1657
- Forero-Romero, J. E., Yepes, G., Gottlöber, S., & Prada, F. 2012, *MNRAS*, 419, 952
- Finkelstein, S. L., Papovich, C., Giavalisco, M., Reddy, N. A., Ferguson, H. C., Koekoemoer, A. M., & Dickinson, M. 2010, *ApJ*, 719, 1250
- Giavalisco, M., et al. 2004a, *ApJ*, 600, L93
- Giavalisco, M., et al. 2004b, *ApJ*, 600, L103
- Grogin, N., et al. 2011, *ApJS*, 197,35
- Hall, N., et al. 2012, *ApJ*, 745, 155
- Hathi, N. P., Jansen, R. A., Windhorst, R. A., et al. 2008, *AJ*, 135, 156
- Hathi, N. P., Ryan, R. E., Cohen, S. H., et al. 2010, *ApJ*, 720, 1708
- Hickey, S., Bunker, A., Jarvis, M. J., Chiu, K., & Bonfield, D. 2010, *MNRAS*, 404, 212

- Ichikawa, T., et al. 2006, SPIE, 6269, 38
- Ichikawa, T., et al. 2007, PASJ, 59, 1081
- Ilbert, O., et al. 2006, A&A, 457, 841
- Kajisawa, M., et al. 2006, PASJ, 58, 951
- Kajisawa, M., et al. 2011, PASJ, 63, S379
- Kinney, A. L., Calzetti, D., Bohlin, R. C., McQuade, K., Storchi-Bergmann, T., & Schmitt, H. R. 1996, ApJ, 467, 38
- Koekemoer, A., et al. 2011, ApJS, 197, 36
- Komatsu, E., et al. 2009, ApJS, 180, 330
- Laidler, V. G., et al. 2007, PASP, 119, 1325
- Madau, P. 1995, ApJ, 441, 18
- Madau, P., Pozzetti, L., & Dickinson, M. 1998, ApJ, 498, 106
- Malhotra, S. 2007, BAAS, 38, 104
- Newman, J. A., Cooper, M. C., Davis, M., et al. 2012, ApJS, submitted (arXiv:1203.3192)
- Oesch, P. A., et al. 2009, ApJ, 690, 1350
- Oesch, P. A., et al. 2010, ApJ, 709, L16
- Oke, J. B., & Gunn, J. E. 1983, ApJ, 266, 713
- Ono, Y., et al. 2012, ApJ, 744, 83
- Ouchi, M., et al. 2009, ApJ, 706, 1136
- Pentericci, L., Fontana, A., Vanzella, E., et al. ApJ, 2011, 743, 132
- Pickles, A. J. 1998, PASP, 110, 863
- Puget, P., et al. 2004, SPIE, 5492, 978
- Renzini, A., et al. 2003, in The Mass of Galaxies at Low and High Redshift, ed. R. Bender, & A. Renzini, 332
- Schenker, M. A., Stark, D. P., Ellis, R., et al. 2012, ApJ, 744, 179

- Stanway, E. R., et al. 2008, MNRAS, 386, 370
- Stark, D. P., Ellis, R. S., & Ouchi, M. 2011, ApJ, 728, L2
- Suzuki, R., et al. 2008, PASJ, 60, 1347
- Trenti, M., & Stiavelli, M. 2008, ApJ, 676, 767
- Trenti, M., et al. 2011, ApJ, 727, L39
- van der Wel, A., et al. 2011, ApJ, 742, 111
- Vanzella, E., Pentericci, L., Fontana, A., et al. ApJ, 730, L35
- Wang, W.-H., Barger, A. J., & Cowie, L. L. 2009, ApJ, 690, 319
- Wang, W.-H., Cowie, L. L., Barger, A. J., Keenan, R. C., & Ting, H.-C. 2010, ApJS, 187, 251
- Wiklind, T., Dickinson, M., Ferguson, H. C., Giavalisco, M., Mobasher, B., Grogin, N. A., & Panagia, N. 2008, ApJ, 676, 781
- Wilkins, S. M., Bunker, A. J., Lorenzoni, S., & Caruana, J. 2011, MNRAS, 411, 23
- Yan, H., et al. 2004, ApJ, 616, 63
- Yan, H., et al. 2005, ApJ, 634, 109
- Yan, H., Windhorst, R., Hathi, N. P., Cohen, S., Ryan, R., O’Connell, R., & McCarthy, P. 2010, RA&A, 10, 867
- Yan, H., et al. 2011, ApJ, 728, L22



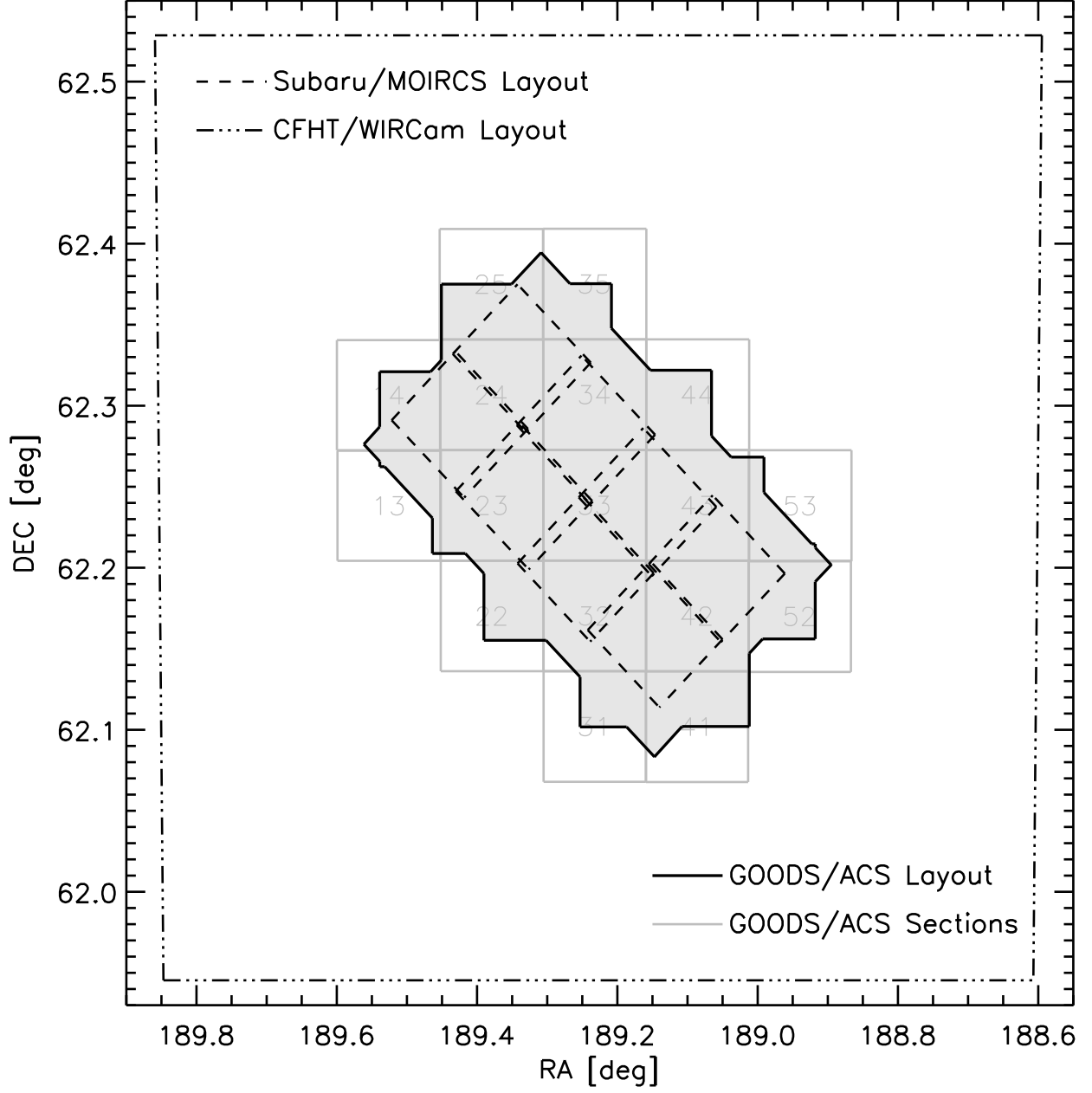


Fig. 1.— The Subaru/MOIRCS (dashed) and the CFHT/WIRCam (large box shown with dot-dash) field layouts in comparison to the GOODS-N ACS (solid) field. The GOODS-N ACS field (a large grid of 40K×40K pixels) was divided into 17 sections (each 8K×8K pixels) for data handling convenience. The gray solid lines show layout of these sections.

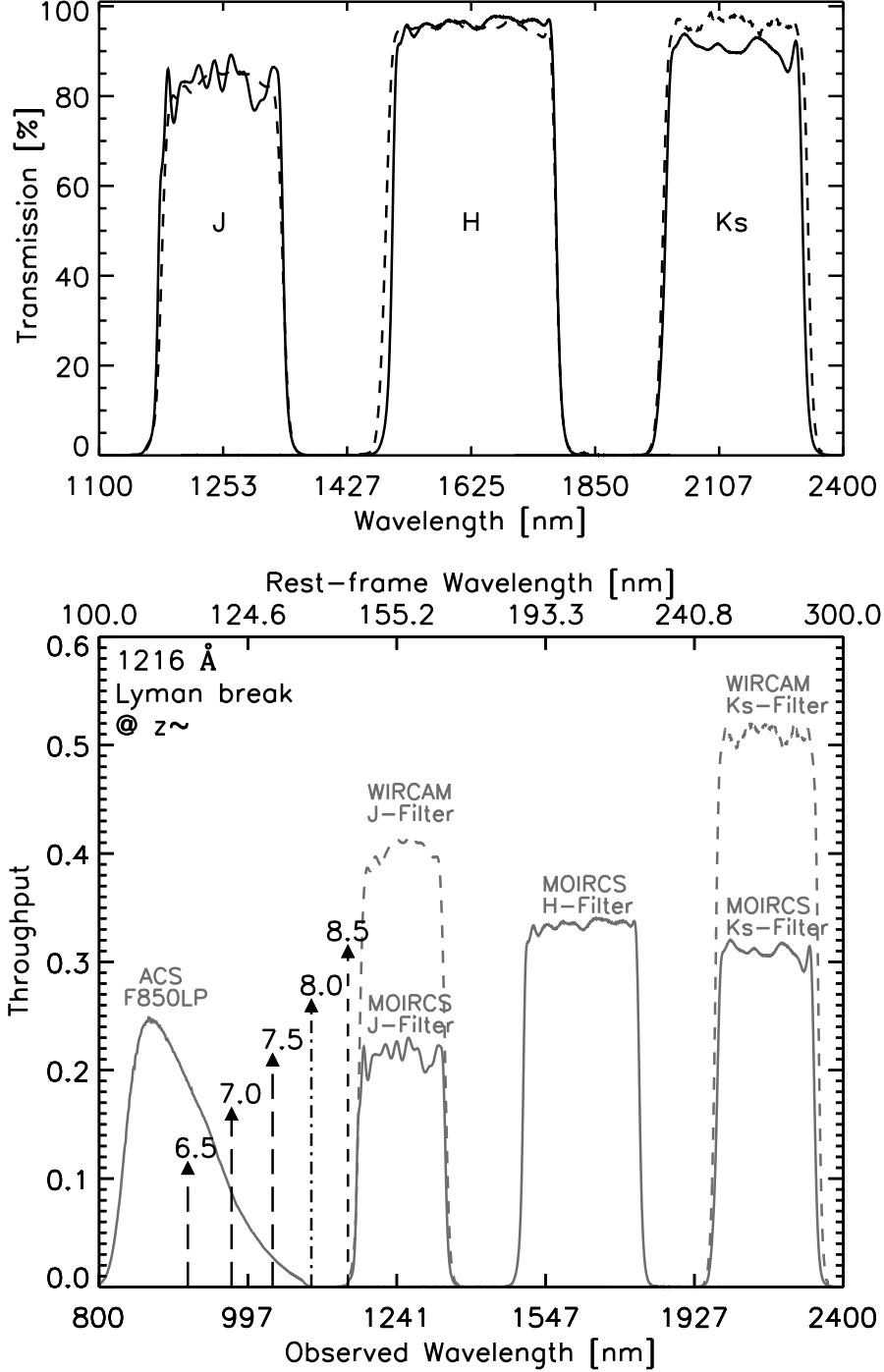


Fig. 2.— [Top] The Subaru/MOIRCS  $J$ ,  $H$ ,  $K_s$  (solid) and the CFHT/WIRCam  $J$ ,  $K_s$  (dashed) filter transmission curves. [Bottom] Location of rest-frame 1216 Å Lyman break at various redshifts ( $z \gtrsim 6.5$ ) and filter throughput curves of  $z_{850}$ -,  $J$ -,  $H$ -,  $K_s$ -bands. The top axis shows corresponding rest-frame wavelengths at  $z \simeq 7$ .

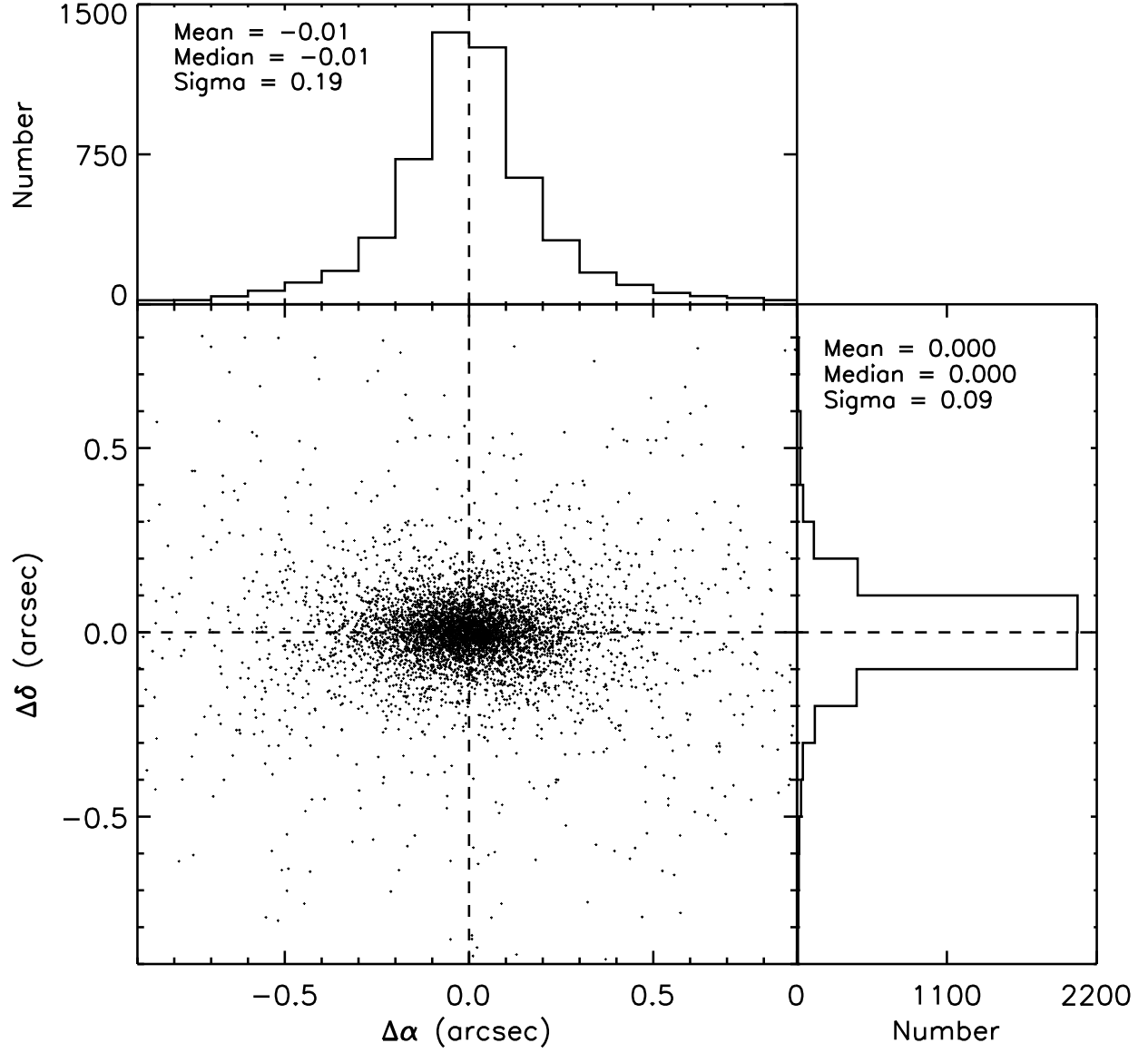


Fig. 3.— Relative astrometric offsets between the combined  $K_s$ -selected and the GOODS-N ACS  $z_{850}$ -selected catalogs. Compact sources with  $S/N > 20$  and  $\text{FWHM} < 1.2''$  are plotted. The histograms show distribution of the offsets in RA and DEC.

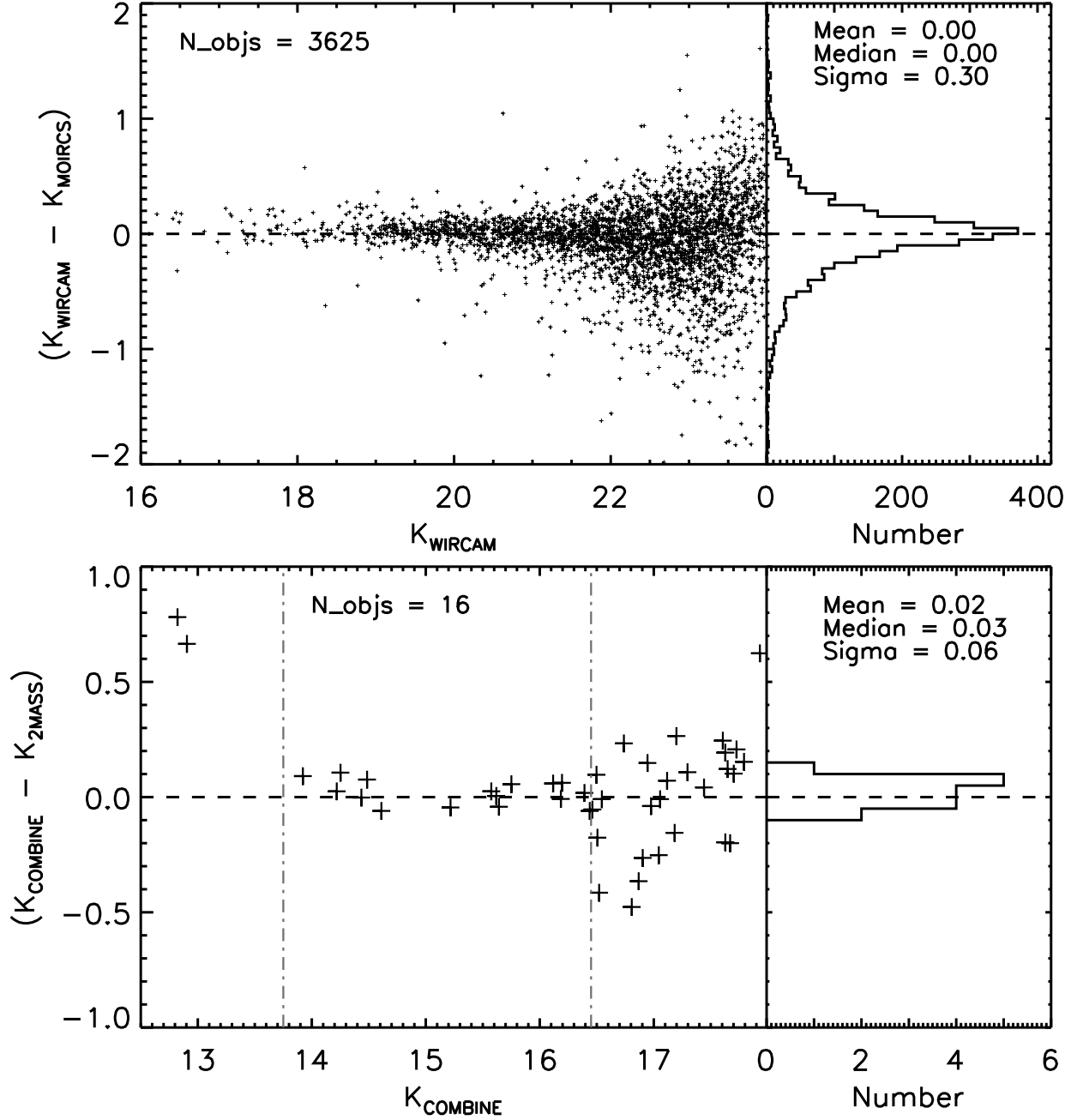


Fig. 4.— [Top] Comparison between  $K_s$ -band magnitudes (`SExtractor` AUTO) obtained from the WIRCam and the MOIRCS images. [Bottom] Comparison between  $K_s$  magnitudes obtained from the combined image and  $K_s$  magnitudes from the 2MASS catalog. We compare 2MASS magnitudes in a magnitude range between  $\sim 14$  and  $\sim 16$  mag (dot-dash vertical lines in the bottom panel) because of the non-linearity/selection issues outside this magnitude range (see Wang et al. 2010, for details).

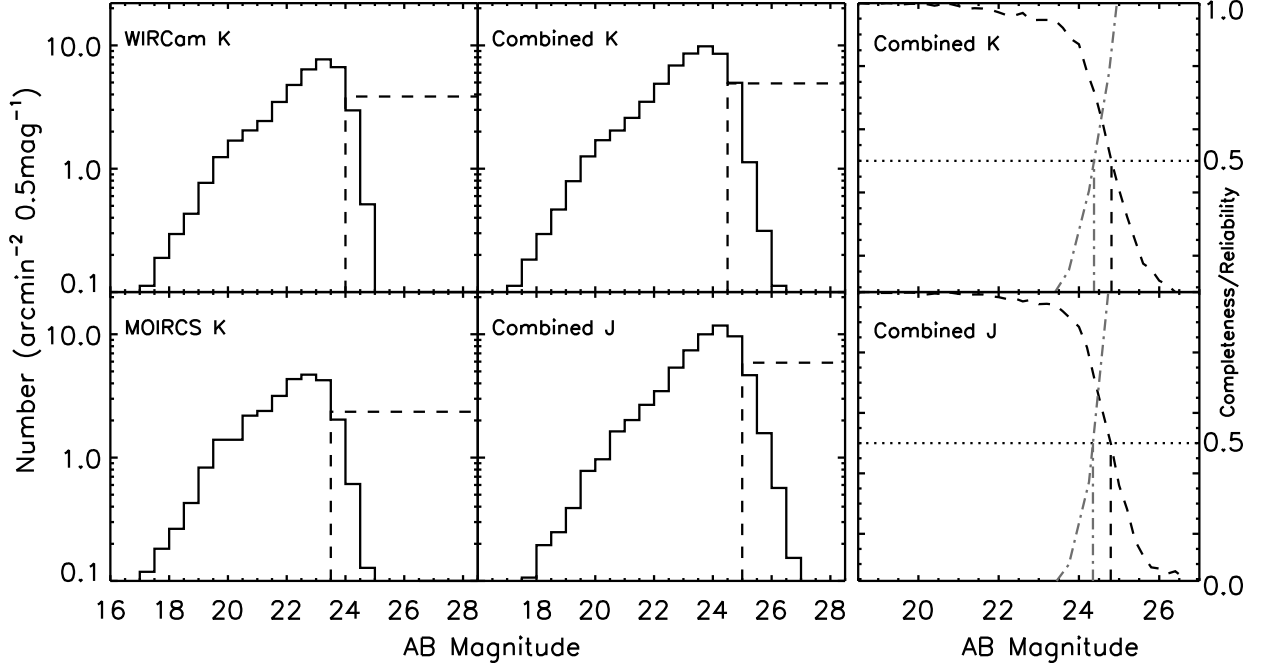


Fig. 5.— [Left 4-panels] The  $K_s$ -band number counts for each image. The bottom-left panels shows MOIRCS  $K_s$ -band number counts, while the top-left panel is for the WIRCam. The bottom-right panel shows  $J$ -band number counts obtained from the combined image, while the top-right panel is for  $K_s$ -band. In all panels, the dashed vertical line shows the magnitude at which the number counts fall to 50% of their peak value. It is clear that combined images are  $\sim 0.5$  mag deeper than the WIRCam or MOIRCS images. [Right 2-panels] The  $K_s$ -band completeness obtained from the simulations. Details of these simulations are discussed in text (§ 4.3). Top panel shows the completeness from the combined  $K_s$ -band image, while the bottom panel is for the combined  $J$ . The dashed vertical line shows the magnitude at which the recovery rate falls to 50%. The dot-dash curve shows the reliability curve (§ 4.3) for both  $J$ - and  $K_s$ -selected catalogs. The dot-dash vertical line shows the magnitude at which the reliability falls to 50%.

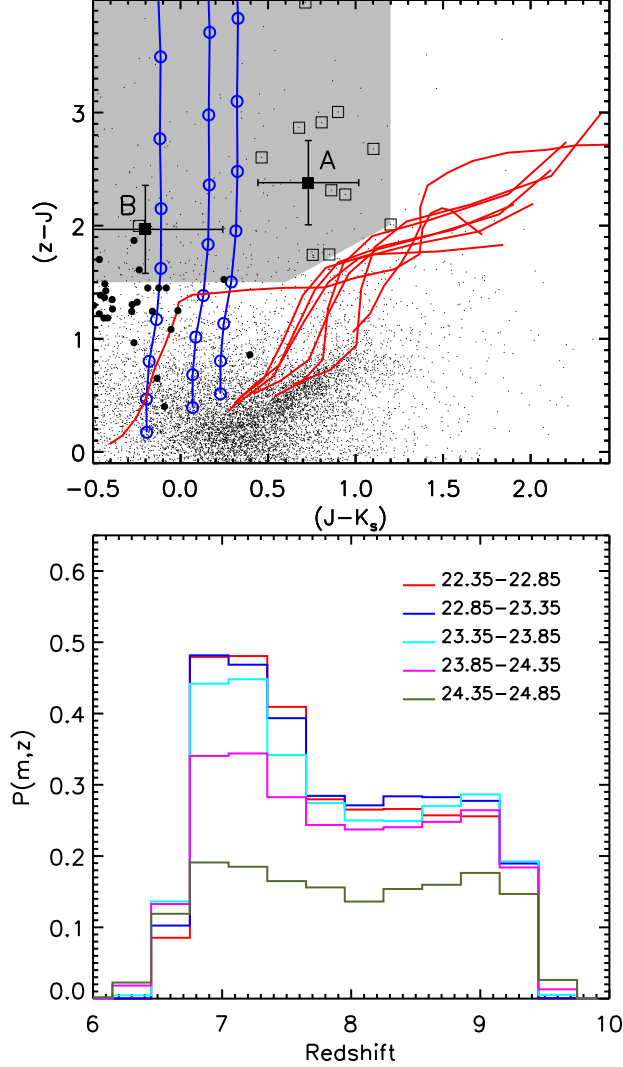


Fig. 6.— [Top] Selection of LBGs at  $z \gtrsim 6.5$  using  $(z-J)$  versus  $(J-K_s)$  colors. The gray shaded region is the selection region. The red curves are BC03, Kinney et al. (1996) and Coleman et al. (1980) model colors of low redshift ellipticals, while blue curves (with open circles indicating different redshifts starting from the bottom  $z=6.0, 6.2, 6.4 \dots$ ) are BC03 models of star-forming galaxies with  $E(B-V)=0, 0.15, 0.30$  mag corresponding to three different curves. The black filled circles are expected colors of late-type stars based on Pickles (1998). The black data points (dots) are *all* objects in the catalog. The filled black squares are two  $z_{850}$ -dropout candidates, and the open black squares are 12 other candidates selected based on this color criteria before checking their *Spitzer* magnitudes and photometric redshifts. The black data points (dots) in the selected region were excluded by other criteria as given in § 5.1. [Bottom] Redshift selection functions at different magnitude bins are shown by color-coded histograms.

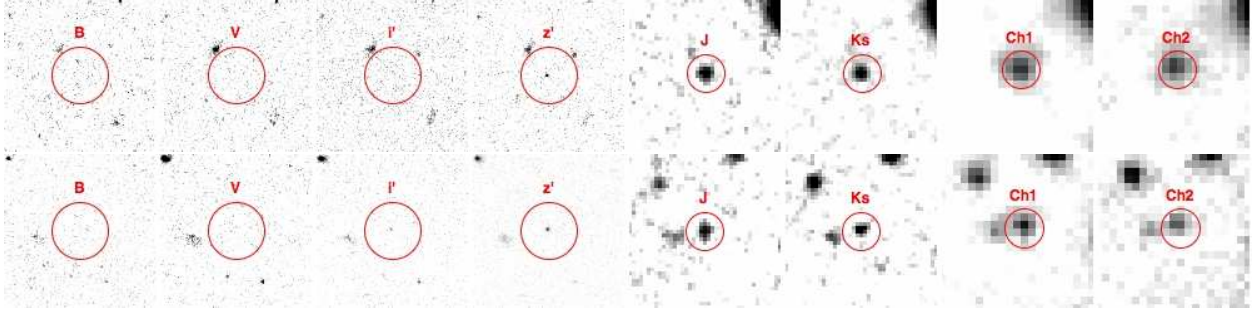


Fig. 7.— Two possible candidates (top panel is candidate A, bottom panel is candidate B) at  $z \gtrsim 6.5$ . The coordinates and photometry of these candidates are shown in Table 3. Left four stamps are ACS  $B_{435}, V_{606}, i_{775}, z_{850}$  images at  $0.06'' \text{ pixel}^{-1}$ , and right four stamps are lower resolution  $J, K_s, [3.6], [4.5]$  images, respectively. The circle shows the position of the object and is  $1.5''$  in radius.

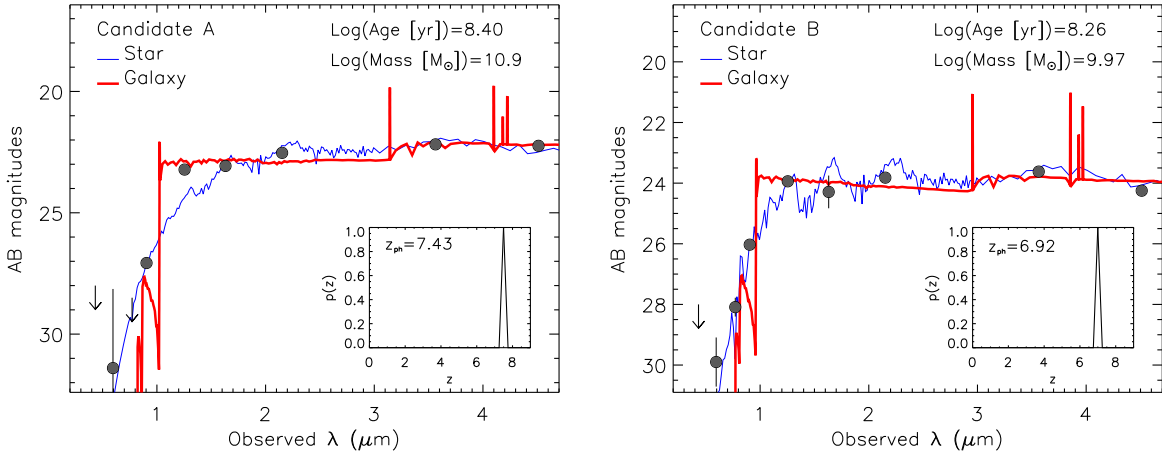


Fig. 8.— Spectral energy distributions of two  $z_{850}$ -dropouts. The stellar SED (blue) and a galaxy SED (red) are shown for each object. Based on these SEDs, Candidate B is equally likely to be a star and a  $z_{850}$ -dropout galaxy. If these candidates are  $z_{850}$ -dropout galaxies then we also show their best-fit stellar ages and stellar masses based on their SED fits. We have used **Le PHARE** (Arnouts et al. 1999; Ilbert et al. 2006) SED/photometric redshift code. The TFIT photometry (except **SExtractor** measured  $H$  mag) is used for SED fitting because it is much more consistent for multi-wavelength data (e.g., Dahlen et al. 2010).

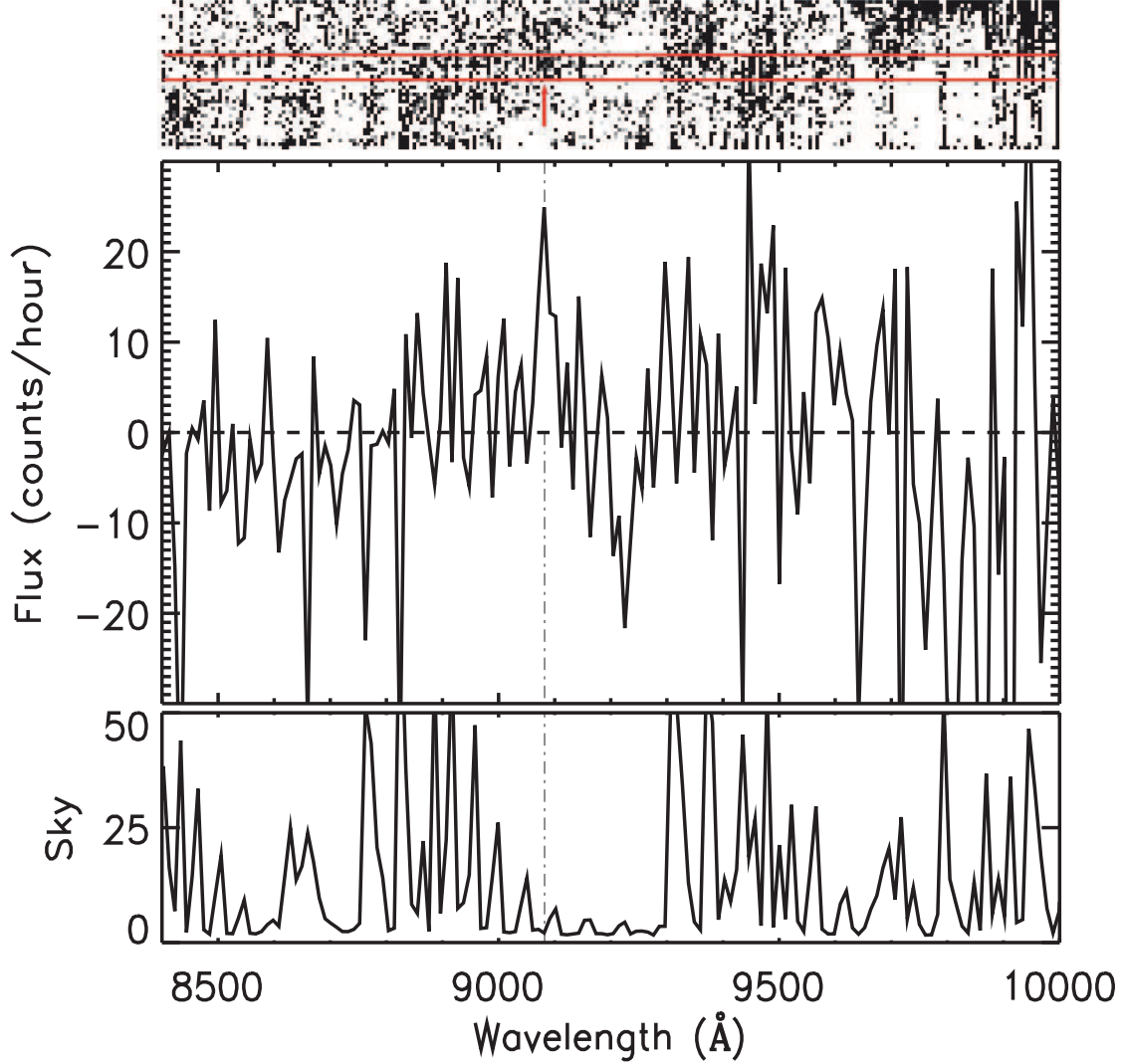


Fig. 9.— [Top] Keck DEIMOS two dimensional spectrum of candidate B covering 8400–10000 Å, displayed using histogram equalization, is shown with the object position bracketed by horizontal red lines. The gray scale is such that the darker is more positive. [Bottom] Corresponding one dimensional spectrum obtain through `spec2d` reduction software. There is a possible weak Ly $\alpha$  line detection at  $\sim 9090$  Å in this spectrum, indicated by a dot-dash line in one dimensional and marked by a red arrow in the two dimensional spectrum. If confirmed, this  $z_{850}$ -dropout candidate could be a LBG at  $z \simeq 6.5$ .



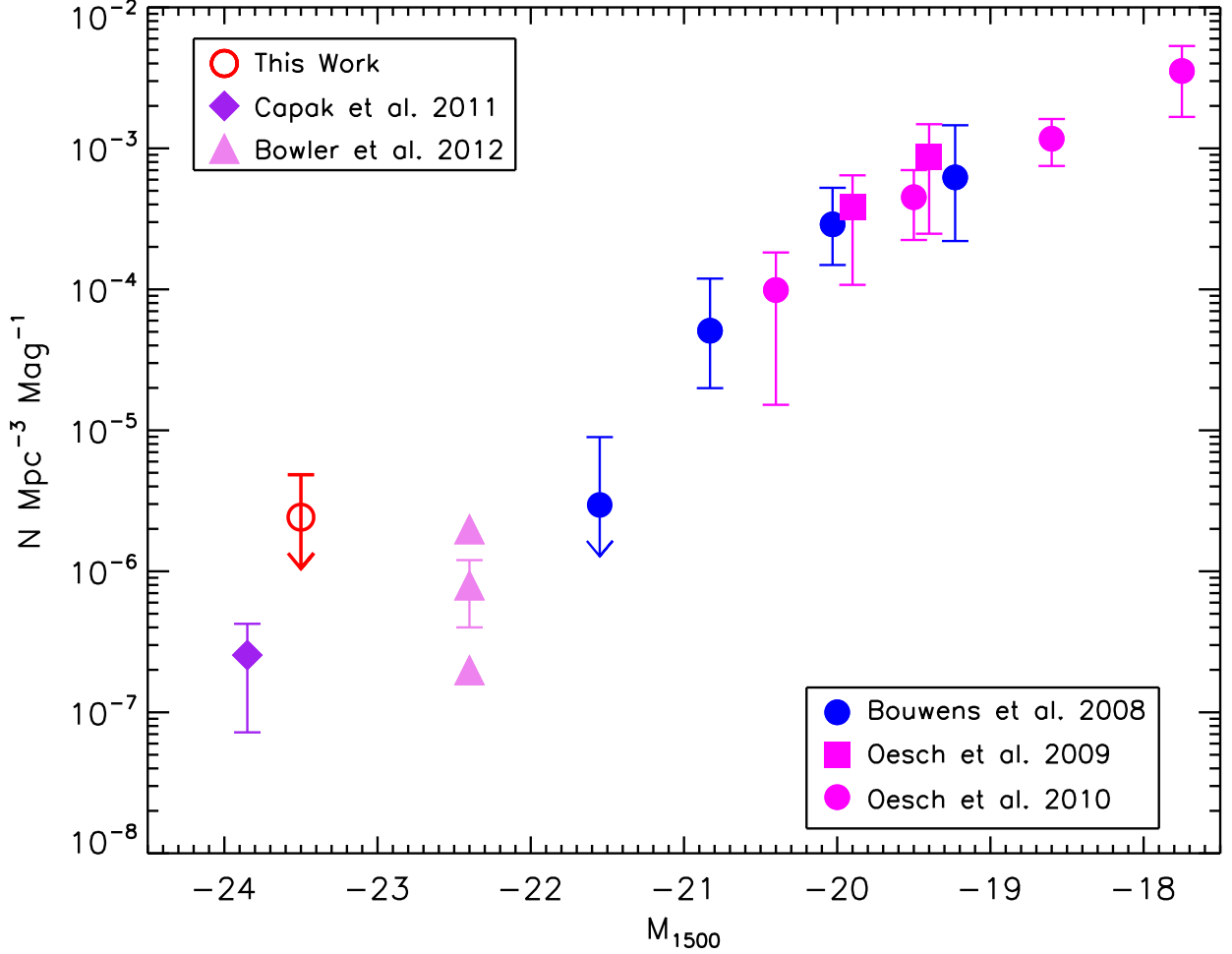


Fig. 10.— Constraints on the bright-end of the luminosity function at  $z \gtrsim 6.5$  (Bouwens et al. 2008; Oesch et al. 2009, 2010; Capak et al. 2011; Bowler et al. 2012) along with our number density based on one possible candidate plotted as open red circle. The upper limit is for two possible candidates, while lower limit (down arrow) means no  $z \gtrsim 6.5$  candidates in this area at this brightness, and the number density has to be less than this value. The small area-deep surveys are not sufficient to probe the bright-end of the luminosity function. We will need wide area surveys (e.g., Trenti et al. 2011; Yan et al. 2011; Grogin et al. 2011) to explore these luminous galaxies at these redshifts.

Table 1. GOODS-N Near-IR data

Telescope/Camera	Filters	Area Coverage (arcmin <sup>2</sup> )	Image Pixel Scale (arcsec pixel <sup>-1</sup> )	Exposure Time <sup>d</sup>	$K_s$ Magnitude Limit <sup>e</sup> (mag)	Typical Seeing (″)
Subaru/MOIRCS	$J, H, K_s$	109	0.15 <sup>a</sup>	~2 hrs	~24.0	0.6-0.8
CFHT/WIRCam	$J, K_s$	1040 <sup>b</sup>	0.30	~3 hrs	~24.0	0.6-0.8
Combined <sup>c</sup>	$J, K_s$	1040 <sup>b</sup>	0.30	~5 hrs	~24.5	0.6-0.8

<sup>a</sup>Native pixel scale is 0.117″ pixel<sup>-1</sup> but to be compatible with other GOODS multi-wavelength data we have used 0.15″ pixel<sup>-1</sup>.

<sup>b</sup>Total WIRCam coverage. For the  $z_{850}$ -dropout selection, we have used only GOODS-N ACS coverage area of ~169 arcmin<sup>2</sup>.

<sup>c</sup>MOIRCS and WIRCam images are combined together to increase the depth in the MOIRCS covered area, which is inside the GOODS-N ACS covered region.

<sup>d</sup>80% of the area has at least this exposure time.

<sup>e</sup>50% completeness limit ( $3\sigma$ ) from Figure 5.

Table 2. **SExtractor** Parameters used for  $K_s$ -selected and  $J$ -selected catalogs. The values in parenthesis are used for  $J$ -selected catalog with other parameters same as  $K_s$ -selected catalog.

Parameter	Value
DETECT_MINAREA	4 (2)
DETECT_THRESH	2.0 (1.0)
ANALYSIS_THRESH	2.0 (1.0)
FILTER	Y
FILTER_NAME	gauss_3.0_5x5.conv
DEBLEND_NTHRESH	32
DEBLEND_MINCONT	0.0001
CLEAN	Y
CLEAN_PARAM	1.0 (0.3)
SEEING_FWHM	0.8
BACK_SIZE	80
BACK_FILTERSIZE	3
BACKPHOTO_TYPE	LOCAL
BACKPHOTO_THICK	12
WEIGHT_TYPE	MAP_RMS

Table 3. Photometry of two  $z_{850}$ -dropout candidates.

ID	RA	DEC	$B_{435}^a$	$V_{606}^a$	$i_{775}^a$	$z_{850}^a$	$J^a$	$H^b$	$K_s^a$	$m_{3.6}^a$	$m_{4.5}^a$	$m_{5.8}^b$	$m_{8.0}^b$	Stellarity <sup>c</sup>	$z_{phot}$
A	189.07061	62.20895	>28.0	31.40	>28.0	27.07	23.22	23.07	22.53	22.18	22.24	22.10	22.04	0.54	7.43
			...	$\pm 3.26$	...	$\pm 0.16$	$\pm 0.06$	$\pm 0.17$	$\pm 0.05$	$\pm 0.01$	$\pm 0.02$	$\pm 0.20$	$\pm 0.21$		
B	189.08286	62.15940	>28.0	29.90	28.09	26.03	23.94	24.29	23.82	23.62	24.25	24.19	>23.75	0.13	6.92
			...	$\pm 0.81$	$\pm 0.31$	$\pm 0.07$	$\pm 0.09$	$\pm 0.54$	$\pm 0.14$	$\pm 0.03$	$\pm 0.08$	$\pm 0.55$	...		

<sup>a</sup>These magnitudes are based on TFIT technique (Laidler et al. 2007; Dahlen et al. 2010).

<sup>b</sup>These magnitudes are based on SExtractor MAG\_AUTO estimates.

<sup>c</sup>Star/Galaxy separation based on SExtractor CLASS\_STAR index (1=star) measured in  $J$ -band.